

Mitigating Internal Instrument Coupling for 21 cm Cosmology. I. Temporal and Spectral Modeling in Simulations

Nicholas S. Kern¹, Aaron R. Parsons¹, Joshua S. Dillon^{1,4}, Adam E. Lanman², Nicolas Fagnoni³, and Eloy de Lera Acedo³

Department of Astronomy, University of California, Berkeley, CA, USA; nkern@berkeley.edu

Department of Physics, Brown University, Providence, RI, USA

Cavendish Astrophysics, University of Cambridge, Cambridge, UK

Received 2019 May 10; revised 2019 August 16; accepted 2019 August 25; published 2019 October 15

Abstract

We study the behavior of internal signal chain reflections and antenna cross coupling as systematics for 21 cm cosmological surveys. We outline the mathematics for how these systematics appear in interferometric visibilities and describe their phenomenology. We then describe techniques for modeling and removing these systematics without attenuating the 21 cm signal in the data. This has critical implications for low-frequency radio surveys aiming to characterize the 21 cm signal from the Epoch of Reionization (EoR) and Cosmic Dawn, as systematics can cause bright foreground emission to contaminate the EoR window and prohibit a robust detection. We also quantify the signal loss properties of the systematic modeling algorithms, and show that our techniques demonstrate resistance against EoR signal loss. In a companion paper, we demonstrate these methods on data from the Hydrogen Epoch of Reionization Array as a proof-of-concept.

Unified Astronomy Thesaurus concepts: Reionization (1383); Cosmology (343); Astronomy data analysis (1858)

1. Introduction

Highly redshifted 21 cm emission from neutral hydrogen in the intergalactic medium (IGM) promises to be a revolutionary tool with which we can study the formation of the first generations of stars and galaxies in the universe and the impact they had on their large-scale environments (Hogan & Rees 1979; Madau et al. 1997; Tozzi et al. 2000). The 21 cm signal is a sensitive, tomographic probe of the astrophysics and cosmology of Cosmic Dawn, or the era of first luminous structure formation, and the Epoch of Reionization (EoR) where ionizing photons from star and galaxy formation ionized all of the neutral hydrogen in the IGM at $z \sim 6$ leftover from recombination (for reviews see Furlanetto et al. 2006; Pritchard & Loeb 2012; Mesinger 2016). The Cosmic Dawn and the EoR are critical components of a broader understanding of large-scale structure formation, yet they remain largely unexplored due to the experimental difficulty of systematically probing the universe at these redshifts across the electromagnetic spectrum.

The prospect of robustly characterizing the 21 cm signal from these epochs is daunting, as galactic and extra-galactic foreground emission outshine the fiducial cosmological signal by many orders of magnitude. Nevertheless, the path toward detecting the 21 cm signal from the Cosmic Dawn and EoR has seen tremendous progress over the past decade, as firstgeneration radio interferometric experiments such as the Donald C. Backer Precision Array for Probing the Epoch of Reionization (PAPER; Parsons et al. 2014; Ali et al. 2015; Jacobs et al. 2015), the Murchison Widefield Array (MWA; Dillon et al. 2014; Beardsley et al. 2016; Ewall-Wice et al. 2016), the Low Frequency Array (Patil et al. 2017), and the Giant Metre Wave Radio Telescope (Paciga et al. 2013) have placed increasingly competitive limits on the 21 cm power spectrum, while single-dish experiments may have made a first detection of the global signal (Bowman et al. 2018). Going forward, second-generation interferometric experiments

like the Hydrogen Epoch of Reionization Array (HERA; DeBoer et al. 2017) and the Square Kilometer Array (Koopmans et al. 2015) are expected to have the raw sensitivity needed to not only detect the 21 cm signal but provide a power spectrum characterization across a wide range of redshifts, leading to dramatic improvements in our understanding of astrophysical and cosmological parameters that govern large-scale structure and star formation at these epochs (Pober et al. 2014; Greig et al. 2015; Greig & Mesinger 2015, 2018; Ewall-Wice et al. 2016; Liu & Parsons 2016; Kern et al. 2017).

Due to the faintness of the cosmological signal, tight control of instrumental systematics is a crucial component of data reduction pipelines. Indeed, many of the upper limits provided by first-generation interferometric experiments have already been systematics limited. As second-generation experiments are constructed and get closer to making a first detection of the 21 cm power spectrum, our ability to model and remove systematics to a high dynamic range will be of utmost importance in maximizing the scientific impact of future 21 cm data sets. Systematic contamination can be generated in a variety of ways, such as calibration errors, ionospheric Faraday rotation, primary beam ellipticity, analog signal chain imperfections (such as impedance mismatches), and others. Generally, their end result is to distort the strong foreground signal in the data, thus making it harder to separate it from the underlying 21 cm signal.

In this work, we focus specifically on a class of systematics that we refer to as *internal instrument coupling*, which we further break down into two subcategories: (1) signal chain reflections or coupling within an antenna signal chain and (2) antenna cross coupling, or coupling between antenna signal chains. Signal chain reflections are generated by impedance mismatches between transmitting surfaces in the analog signal chain when the signal is carried as a voltage. Their effect is to generate a copy of the foreground signal in a region of k space nominally occupied only by the EoR 21 cm signal and thermal noise. Cross coupling, on the other hand, can occur from a variety of mechanisms, but common sources for radio surveys are stray capacitance between parallel wires or circuit lines in

⁴ NSF Astronomy and Astrophysics Postdoctoral Fellow.

the signal chain (i.e., capacitive crosstalk) and reflections between antennas in the field (i.e., mutual coupling). Cross coupling produces a spurious phase-stable term in the data across time that can occupy a wide range of k modes, depending on its origin. These systematics are of critical concern for low-frequency radio surveys (Parsons et al. 2012; Zheng et al. 2014; Chaudhari et al. 2017), and have proven to be a partially limiting factor in previous 21 cm interferometric analyses (Beardsley et al. 2016; Ewall-Wice et al. 2016). We use HERA sky and systematic simulations to study the temporal and spectral behavior of internal coupling systematics in the context of HERA data, and propose techniques for modeling and removing them from the interferometric data products. We furthermore quantify the signal loss properties of our algorithms with ensemble subtraction trials containing simulated EoR observations. In this work we do not simulate the effects of thermal noise, as we aim to probe the inherent algorithmic performance to a very high dynamic range, however, we discuss the anticipated impact of thermal noise on our algorithms in Section 3.

Recently, Tauscher et al. (2018) studied systematic removal for 21 cm survey data using a simulation-based, forward-model approach for separating systematics from the EoR signal. This seems to work well when the systematic parameter space is fairly limited and the systematic itself well understood: in their case they consider only beam-weighted foregrounds as a systematic, with a few parameters governing its spatial and spectral dependence. Our work takes a semiempirical approach to modeling instrument systematics due to (1) the highly variant nature of the systematics observed in the real data, and (2) because we require suppression to high dynamic range, which is often more easily achieved with flexible empirical methods. The consequence of using semiempirical systematic models is that they can be overfit and induce loss of EoR signal, which we test for in this work.

The structure of this paper is as follows. In Section 2 we provide a mathematical overview of how the two systematics described in this paper corrupt interferometric data products, and make predictions for their spectral and temporal behavior. In Section 3 we introduce algorithms for modeling and removing these systematics from the data, and then use simulated HERA data with and without systematics to test the performance of our techniques. In Section 4 we validate our algorithms by quantifying their signal loss properties, ensuring they are not lossy to the desired EoR sky signal. Lastly, in Section 5 we summarize our results. In a companion paper, Kern et al. (2019), we demonstrate the performance of these techniques on real data from the HERA Phase I instrument. Many of the assumptions made in this work about the functional form of the simulated systematics come from the actual observed systematics outlined in that paper.

2. Mathematical Overview

In this section, we describe how signal chain reflections and antenna cross couplings appear in interferometric data products. To begin, we start with a the two-element interferometer (Hamaker et al. 1996; Smirnov 2011), consisting of two antennas, 1 and 2, whose feeds measure an incident electric field and convert it into a voltage. In Figure 1, we show a schematic of the HERA analog system and mark possible sources of internal instrument coupling. These signals travel from the feeds through each antenna's signal chain to the correlator, and along the way are amplified, digitized, channelized, and Fourier transformed into the frequency domain.

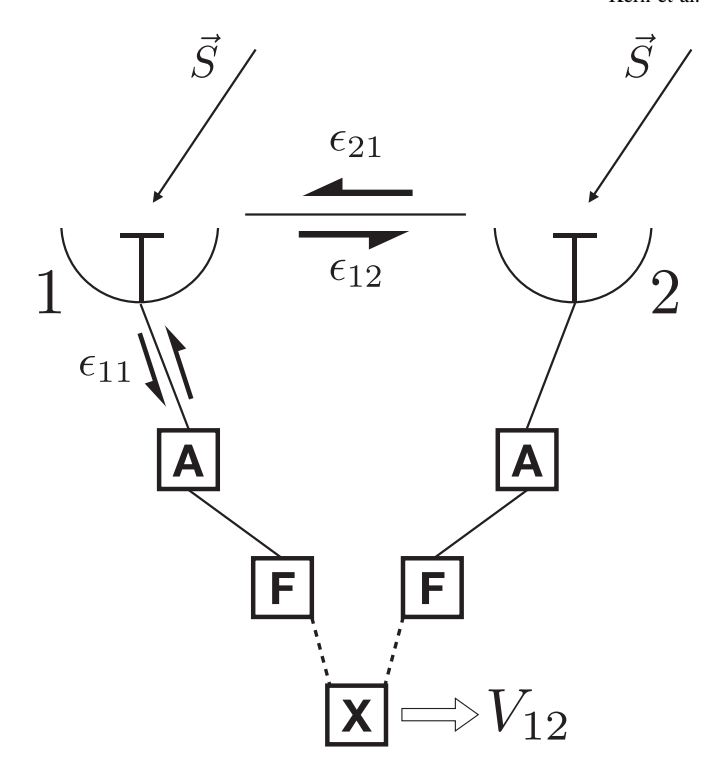


Figure 1. A schematic of two HERA signal chains, 1 and 2, with possible sources of systematics demarcated. Sky signal (\mathcal{S}) enters each antenna's feed, is converted into a voltage and travels down their signal chains where it is first processed at a node housing an amplifier (A). It is then directed to an engine that digitizes and Fourier transforms the signal (F) and sent to the correlator (X), which produces the visibility V_{12} . A possible cable reflection in antenna 1's signal chain is marked as ϵ_{11} , traversing up and down the cable connecting the feed to the node, and possible cross coupling is marked as ϵ_{12} , where radiation is reflected off of antenna 2 and into antenna 1, or vice versa. Dashed lines indicate a signal pathway after digitization, where internal instrument coupling is no longer a major concern.

The correlator then cross multiplies voltage spectra to form the fundamental interferometric data product: the cross-correlation visibility, V_{12} , between antenna 1 and 2, written as

$$V_{12}(\nu, t) = v_1(\nu, t)v_2^*(\nu, t). \tag{1}$$

The correlator can also produce the autocorrelation visibility by correlating an antenna voltage with itself (e.g., V_{11}). Here we have chosen to define the visibility as the product of two antenna voltage spectra, rather than the correlation of voltage time streams: although the two are equivalent given the convolution theorem, the former will prove to be an easier basis when working with reflections. In addition, we have been explicit about the frequency and time dependence of each antenna's voltage spectrum v, and by extension, the complex visibility V, although we drop these throughout the text for brevity. We have also dropped the time averaging done by any real correlator, which is done for brevity and does not alter our results in this section. While we could have cast the visibility equation (Equation (1)) in matrix form (e.g., Hamaker et al. 1996; Smirnov 2011), we find it easier to understand the impact that the specific systematics we discuss in this paper have on the resultant data products using a simpler, algebraic form for the visibility equation.

The correlator outputs time-ordered visibilities as a function of local sidereal time (LST; denoted as t) and frequency

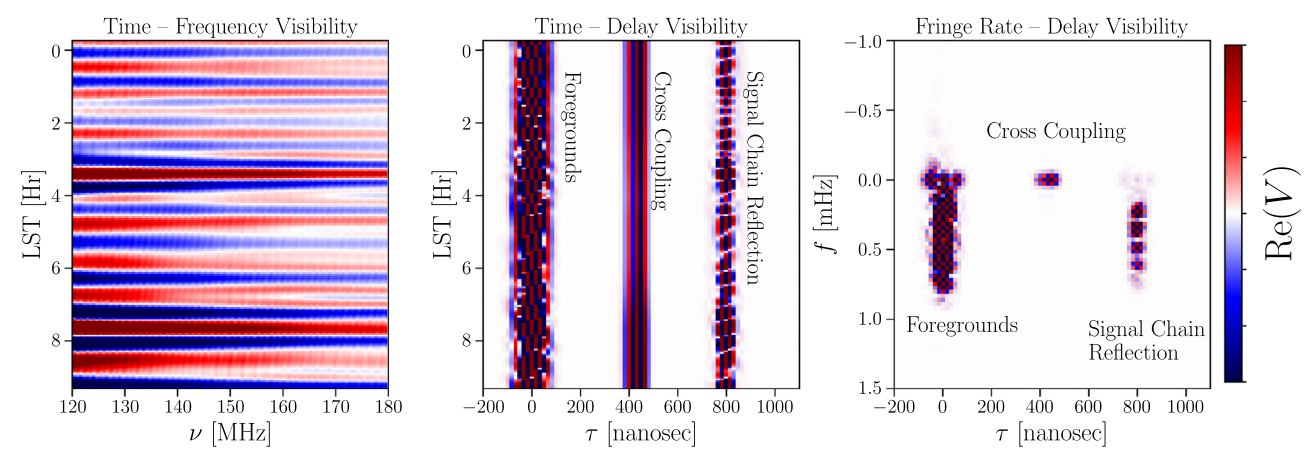


Figure 2. The real component of a simulated cross-correlation visibility with foregrounds, a signal chain reflection inserted at $\tau=800$ ns, and a cross-coupling term inserted at $\tau=400$ ns, plotted in dimensionless units for visual clarity. Left: visibility in time and frequency space. Center: visibility in time and delay space. Right: visibility in fringe rate and delay space. Different components of the visibility—in particular systematics—are usually better separated in delay and fringe-rate space than in the original time and frequency space.

(denoted as ν). When Fourier transforming the data across the frequency axis, we put the data into a temporal domain. To separate this from the original time domain, we refer to the Fourier dual of frequency as the *delay domain* (denoted as τ). Similarly, the Fourier transform of our data across time puts the data into a spectral domain, which we refer to as the *fringe-rate domain* (denoted as f), using similar notation as that used by Parsons et al. (2016). In the absence of explicit markers, we will use V to mean the visibility in time and frequency space, and use \widetilde{V} to mean the visibility in one or both of the Fourier domains, which should be clear based on context, otherwise we will use explicit notation.

Different components of the visibility are generally more localized in Fourier space. Foreground signal, for example, is intrinsically spectrally smooth and will therefore occupy low delay modes, whereas a fiducial EoR model, being nonspectrally smooth, occupies low and high delay modes. Figure 2 shows a simulated foreground + systematic visibility in real and Fourier space, demonstrating how systematics are usually better separated in Fourier spaces (center and right panel). We present the figure here to guide the reader's intuition about the phenomenology of the systematics in real and Fourier space while we discuss their mathematical form below. Note that the parameters of the systematics as simulated in Figure 2, for example, the delays they show up at, have been chosen merely for visual clarity, and are not necessarily the systematic parameters seen in actual data. We describe the simulations used throughout this work in Appendix A.

2.1. Describing Signal Chain Reflections

A reflection in the signal chain of an antenna inserts a copy of the original signal with a time lag. An example of this is a reflection at the end of an analog cable, where the signal travels back up the cable, reflects again at the start of the cable, and travels back down and is transmitted through the system along with the original signal. The time lag, or delay, the reflected signal has acquired is two times the cable length divided by the speed of light in the cable. The reflected signal also acquires an amplitude suppression, meaning that it is generally only a fraction of the input signal, but even a small fraction of the foreground signal in the data can dwarf the expected EoR signal and therefore needs to be accounted for. If v_1 is antenna

1's voltage spectrum without a signal chain reflection, then the presence of a reflection can be encapsulated as

$$v_1'(\nu, t) = v_1(\nu, t) + \epsilon_{11}(\nu)v_1(\nu, t), \tag{2}$$

where v_1' is the voltage spectrum of antenna 1 with the reflection component, and ϵ is a coupling coefficient describing the reflection in antenna 1's signal chain (denoted as 11 because it is coupling the signal with itself). The coupling coefficient can be broken into three constituent parameters as

$$\epsilon_{11}(\nu) = A_{11}e^{2\pi i \tau_{11}\nu + i\phi_{11}},$$
(3)

where A is the amplitude, τ is the delay offset (the total time it takes to be reflected), and ϕ is the phase offset the reflected signal may have acquired relative to the original signal. In Equation (2) we have assumed time and frequency stability of the reflection parameters, although in practice these parameters will have some variation with time and frequency.

If we insert the corrupted voltage spectra into the visibility equation (Equation (1)), we get

$$V_{12}' = v_1 v_2^* + \epsilon_{11} v_1 v_2^* + v_1 \epsilon_{22}^* v_2^* + \epsilon_{11} v_1 \epsilon_{22}^* v_2^*. \tag{4}$$

We can see that in addition to the original cross-correlation term $(v_1v_2^*)$ we now also have copies of it at positive and negative delay offsets that are suppressed in amplitude by a factor of A_{11} and A_{22} , respectively. The time behavior of a reflection mimics that of the original data, in that it shows the same temporal oscillation (i.e., fringing) as the foregrounds, and thus also appears at the same fringe-rate modes as the foregrounds (e.g., right panel of Figure 2). The conjugation of ϵ_{22} means that the reflected signal from antenna 2 appears at negative delays in V_{12} , while the reflected signal from antenna 1 appears at positive delays.

The resultant autocorrelation visibility can also be computed, and is given by

$$V'_{11} = v_1 v_1^* + \epsilon_{11} v_1 v_1^* + v_1 \epsilon_{11}^* v_1^* + |\epsilon_{11}|^2 v_1 v_1^*, \tag{5}$$

where we see that the first-order reflections show up at $\pm \tau_{11}$, while the second-order reflection appears at $\tau = 0$ ns, due to

the conjugation of the coupling coefficient with itself. If we assume that the first-order reflections are at sufficiently high delay and neglect the second-order term, we can approximate the visibility at $\tau=0$ ns as $\widetilde{V}'_{11}(\tau=0)\approx (v_1v_1^*)(\tau=0)$. Similarly, near the reflection delay of τ_{11} the autocorrelation visibility simplifies to

$$\widetilde{V}_{11}'(\tau=\tau_{11})\approx\epsilon_{11}v_1v_1^*.$$
 (6)

This means that one can estimate the reflection coefficient amplitude in delay space as

$$A_{11} = \frac{|\widetilde{V}'_{11}(\tau = \pm \tau_{11})|}{|\widetilde{V}'_{11}(\tau = 0)|},\tag{7}$$

which will be useful when modeling reflection systematics.

If one can estimate their parameters from the data, reflections can be removed via standard (direction-independent) antenna-based calibration. In this paradigm, the raw voltage spectrum of antenna 1 corrupted by the instrument is related to its true value as

$$v_1^{\text{raw}} = v_1 g_1, \tag{8}$$

which when inserted into the visibility equation yields the standard antenna-based calibration equation,

$$V_{12}^{\text{raw}} = V_{12} g_1 g_2^* = \langle v_1 v_2^* \rangle g_1 g_2^*. \tag{9}$$

The *g* term is called the antenna gain, and accounts for amplitude and phase errors introduced by the various stages of the signal chain from the feed all the way to the correlator. Note that this form of the calibration equation does not account for polarization leakage induced by cross-feed coupling, which is generally a higher order correction (Hamaker et al. 1996; Sault et al. 1996). By rearranging Equation (2) as

$$v_1' = v_1(1 + \epsilon_{11}) = v_1 g_1,$$
 (10)

we can see that signal chain reflections can be completely encompassed in this gain term, and hence corrected for by dividing the corrupted data by a gain constructed from an estimate of the reflection coefficient.

2.2. Describing Antenna Cross Coupling

We now turn our attention to another systematic we refer to as antenna cross coupling, which acts to couple one antenna's voltage stream with another antenna's voltage stream before reaching the correlation stage. Note that our model for cross coupling is different than "capacitive crosstalk" created by the electric field of two parallel signal chains interacting with each other within cabling, receivers, and analog-to-digital conversion units, which is a common systematic for radio interferometers (Parsons & Backer 2009; Zheng et al. 2014; Ali et al. 2015; Patil et al. 2017; Cheng et al. 2018). There are well-established hardware solutions for suppressing crosstalk, such as phase switching (Chaudhari et al. 2017). However, if residual crosstalk remains, or if phase switching is not implemented in the system, we need to model and remove it for robust EoR measurements.

Our cross coupling systematic model simply states that, before correlation, one antenna's voltage is added to another antenna's voltage with a coupling coefficient that determines the amplitude and relative delay with which the voltage is

added. For the purposes of our description, we additionally assume that this coupling coefficient can be decomposed into the same three parameters as before, technically making it a form of reflection systematic.⁵ While this model may indeed be capable of describing certain some forms of capacitive crosstalk, we do not expect all forms of capacitive crosstalk to necessarily fall within the bounds of these assumptions.

To write down how this affects the interferometric visibility, we can start by writing the corrupted antenna voltages as

$$v_1' = v_1 + \epsilon_{21} v_2 v_2' = v_2 + \epsilon_{12} v_1,$$
(11)

where ϵ_{21} describes the voltage coupling of antenna 2 into antenna 1 and vice versa for ϵ_{12} . Substituting these equations into Equation (1), we get

$$V_{12}' = v_1 v_2^* + v_1 \epsilon_{12}^* v_1^* + \epsilon_{21} v_2 v_2^* + \epsilon_{21} v_2 \epsilon_{12}^* v_1^*. \tag{12}$$

We can see that the cross-correlation visibility now contains the autocorrelation visibility terms $v_1v_1^*$ and $v_2v_2^*$ at the first-order level, which are purely real quantities and thus have identically zero phase. In the complex plane, the cross-correlation term $v_1v_2^*$ winds around the origin as a function of time because its phase varies temporally. Because the autocorrelation has no phase, the act of the cross-coupling terms is to introduce an additive bias to the data with an arbitrary phase set by the coupling coefficient itself. Assuming the coupling coefficient is slowly variable (if not completely stable), the first-order systematic terms in Equation (12) only change in amplitude over time set by the natural variation in the amplitude of the autocorrelation, (e.g., $v_1v_1^*$). This variation is generally fairly slow on timescales of a beam crossing, which for HERA is roughly 1 hr. This leads us to two critical insights about the behavior of the cross-coupling terms: (1) their time variability is slow, thus occupying low-fringe rate modes (e.g., see right of Figure 2) and (2) they have a time-stable phase determined solely by the phase of the coupling coefficient.

In a more generalized case, the cross coupling between antenna 1 and 2 may have an angular dependence on the sky. Take for example the case of mutual coupling (or feed-to-feed reflections), where part of the radiation incident on antenna 1's feed is reflected and received by antenna 2's feed. This behavior will be highly angular dependent due to the nontrivial electromagnetic properties of the feed itself. Nonetheless, we can reason that the systematic phenomenology will be similar to as before. We can think of this angular dependence as a windowing function on the primary beam of the underlying autocorrelation, meaning that the first-order terms in Equation (12) will be proportional to only a fraction of $v_1v_1^*$, such that they have a smaller amplitude. It may also mean that these terms will have a slightly faster time dependence in the data, as the "effective beam" created by the angular windowing function is smaller on the sky than the total primary beam, and thus leads to a faster "effective beam crossing time."

⁵ While we adopt this assumption in this section to make the algebra simpler, the algorithm we present in Section 3 is more general and does not rely on this assumption.

We can also compute the effects of cross coupling on the measured autocorrelation visibility, V_{11} , which yields

$$V'_{11} = v_1 v_1^* + v_1 \epsilon_{21}^* v_2^* + \epsilon_{21} v_2 v_1^* + |\epsilon_{21}|^2 v_2 v_2^*. \tag{13}$$

In this case, we find that the cross correlation is inserted into the measured autocorrelation at the first-order level with a delay offset of τ_{21} . These terms are likely many order of magnitudes below the peak autocorrelation visibility amplitude, given that the cross-correlation visibilities are generally a few orders of magnitude below the autocorrelation inherently, which is further compounded by the amplitude suppression from ϵ_{21} .

We can see simply from Equation (12) that the corruption of V'_{12} by cross coupling *cannot* be factorized into antenna-based gains, based simply on the presence of the ϵ_{12} -like terms, which are baseline dependent. Removal of cross-coupling terms in the data must therefore be done on a per-baseline basis by constructing a model of the systematic in each visibility and then subtracting it.

2.3. Summary

To summarize, reflections along a single antenna's signal chain produces a duplicate of the signal with suppressed amplitude and some delay offset. This is true for both the cross-correlation and autocorrelation visibility products. Example mechanisms include cable reflections and dish-to-feed reflections within the confines of a single antenna. Reflections in the cross-correlation visibility have the same time structure as the un-reflected visibility, meaning reflected foreground signal occupies the same fringe-rate modes as un-reflected foreground signal, but is shifted to high delays (e.g., Figure 2). Reflections can be removed from the raw data by creating a model of the reflections and incorporating them into the per-antenna calibration gains.

Another systematic we describe is created by antenna-to-antenna cross coupling, which mixes the voltage signals between the antennas. This has the effect of introducing a copy of the autocorrelation visibility into the measured cross-correlation visibility at positive and negative delay offsets, and similarly introduces copies of the cross-correlation visibility into the measured autocorrelation visibility. In the measured cross-correlation visibility, the first-order coupling terms are slowly time variable and occupy low-fringe-rate modes centered at f=0 Hz. Cross-coupling terms cannot be removed via antenna-based calibration, and must be modeled and subtracted at the per-baseline level.

3. Systematic Modeling

Next we discuss our approach for modeling reflection and cross-coupling systematics in the data. We use sky and instrument simulations to generate mock visibilities of diffuse foregrounds and systematics, which we use to test our algorithms and provide benchmarks on their performance. More details on the construction of the simulated data products used in this work can be found in Appendix A. The fiducial parameters of our systematic simulations are chosen to roughly reflect the behavior of systematics seen in HERA Phase I data (Kern et al. 2019). Systematics in the HERA Phase I system can be found at variable amplitudes and delays in the data, depending on the baseline or antenna at hand, but are generally seen at an amplitude of $\sim 3 \times 10^{-3}$ times the peak foreground amplitude at $\tau=0$ ns and at delays spanning 200–1500 ns. For these simulations we do not

include instrumental thermal noise so that we can test the underlying performance of our algorithms to a high dynamic range.

3.1. Modeling Signal Chain Reflections

Modeling signal chain reflections can in theory be done simultaneously with standard gain calibration because reflections factor as an antenna-based effect (see Section 2). However, there are reasons why we might be wary of using standard calibration techniques for deriving reflection parameters. Principally, standard bandpass calibration typically operates on the $\sim N_{\rm ant}^2$ number of cross-correlation visibilities, and generally allows each frequency channel's gain to be solved independently from other channels. Frequency-dependent calibration errors will therefore set a fundamental floor to the precision with which reflections can be calibrated via standard antenna-based bandpass techniques (Barry et al. 2016; Ewall-Wice et al. 2017; Orosz et al. 2019). Furthermore, the dynamic range of the signal to noise is considerably higher in the autocorrelation than in the cross-correlation visibility, as it is a measurement of the total power received by an antenna: in many cases a signal chain reflection cannot even be seen above the noise floor in a cross-correlation visibility but is highly apparent in the autocorrelation visibility. This latter point is important, because it implies that reflection parameters estimated from the autocorrelation visibilities will have a signal-to-noise ratio (S/N) that is drastically higher than the S/N of the cross-correlation visibilities, meaning that, when calibrating out systematics in the cross-correlation visibilities, the S/N of the derived reflection parameters will never be a limiting factor. Of course other real-world factors can limit the precision of the derived reflection parameters such as nontrivial frequency evolution, which is discussed in more detail in the context of HERA in Kern et al. (2019).

Reflection parameters must be estimated to high precision in order to get even a modest suppression of their systematic power in the visibilities. For example, Ewall-Wice et al. (2016) employed a reflection fitting algorithm on MWA autocorrelation visibilities by fitting sinusoids in the frequency domain and was able to suppress reflection systematics by a couple orders of magnitude in the power spectrum, although their end-result band powers were still systematic limited at some *k* modes. Similarly, Beardsley et al. (2016) explored reflection calibration on MWA data as an extension to their restricted polynomial gain calibration scheme and also achieved a couple of orders of magnitude of suppression in the 2D power spectrum, although their more deeply integrated power spectra show its reemergence.

The algorithm we present here also operates on the autocorrelation visibility, but we choose to model the reflection in the delay domain rather than the frequency domain. Recall from Section 2 that in the autocorrelation visibility, V_{11} , a signal chain reflection appears as a shifted copy of the original visibility at symmetric positive and negative delay offsets. The Fourier transformed autocorrelation visibility, $|\tilde{V}_{11}|$, is intrinsically quite peaky in delay space, meaning that a reflection is essentially a narrow spike appearing at its corresponding reflection delay. The reflection amplitude is then estimated via Equation (7), and the reflection phase is estimated by transforming back to frequency space and aligning reflection templates while varying their phase until a squared error metric is minimized. This yields an initial estimate of the reflection

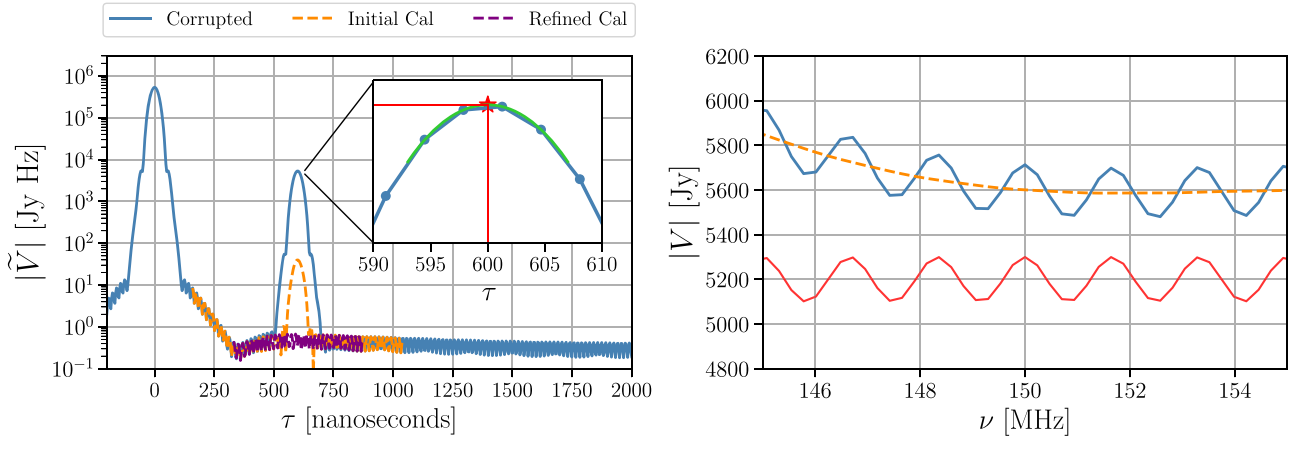


Figure 3. Reflection modeling and removal on a simulated autocorrelation visibility. Left: foreground-only autocorrelation in delay space with a simulated cable reflection at 600 ns (blue line). The orange-dashed line shows the visibility after initial reflection calibration, demonstrating roughly two orders of magnitude of suppression. The inset highlights the reflection bump, showing a spectral fit via quadratic interpolation (green curve) to achieve more precise estimates of the reflection delay and amplitude (red star). The calibration is then refined using an iterative technique until the reflection bump is minimized (purple). Right: simulated visibility with reflection in frequency space (blue line), a scaled version of the fitted reflection coefficient (red line) highlighting its phase coherence with the reflection ripple in the data, and the visibility after initial calibration (orange-dashed line).

parameters, but it needs to be refined in order to suppress the systematic to high dynamic range. In order to refine our parameter estimates, we set up a nonlinear optimization system that perturbs the initial guesses, applies the calibration to the data in frequency space, transforms to Fourier space, estimates the amplitude of the residual reflection bump, and repeats until it is minimized or a stopping threshold is reached. Solving this with an iterative minimization technique allows us to estimate the reflection parameters with sufficient accuracy to suppress the reflection in our systematic simulations by eight orders of magnitude in the power spectrum.

To summarize, our approach for estimating the reflection parameters from the data takes the following steps:

- 1. Zero-pad the autocorrelation in frequency space and apply a windowing function before Fourier transforming to delay space to minimize sidelobe power.
- 2. Fit for the peak of the reflection bump in $|\widetilde{V}|$ via quadratic interpolation of its nearest neighbors.
- 3. The estimated reflection delay, τ , is equal to $\tau_{\rm peak}$.
- 4. The estimated reflection amplitude, A, is the ratio $|\widetilde{V}(\tau = \tau_{\text{peak}})|/|\widetilde{V}(\tau = 0)|$ (Equation (7)).
- 5. Set all modes of \widetilde{V} to zero except the modes nearest $au_{\rm peak}$ and Fourier transform back to frequency space to get $V_{\rm filt}$.
- 6. The estimated reflection phase, ϕ , is found by minimizing $|V_{\text{filt}} Ae^{2\pi i \nu \tau + i\phi}|^2$ while varying ϕ from 0 to 2π .
- 7. Set up a nonlinear optimization that perturbs the initial reflection parameter estimates, applies the calibration and transforms to Fourier space until the residual near the original reflection bump is minimized or a stopping threshold is reached.

We demonstrate this algorithm on a simulated HERA autocorrelation visibility corrupted by a cable reflection with a (frequency-independent) amplitude of 10^{-2} at a delay of 600 ns (Figure 3). The natural delay resolution of HERA data is 10 ns, which is much too coarse to achieve precision estimates of the reflection delay. Zero-padding the data by a factor of three gets us to a delay resolution of 3 ns, but this is still not precise enough for accurate reflection delay estimates. By employing quadratic interpolation on the spectral peak, we can recover the input cable delay to roughly ± 0.1 ns (left of

Figure 3). In this idealized, noise-free simulation, the initial reflection calibration estimates the reflection delay to within ± 0.1 ns of its true value, and its phase to within ± 0.01 radians, yet we only see systematic power suppression of two orders of magnitude in the visibilities. This is representative of the precision needed to achieve even modest systematic suppression. With the refined reflection calibration, however, we find we can achieve reflection systematic suppression of up to four orders of magnitude in the visibility, and recover the reflection parameters to within 1 part in 10^6 of their true value.

Fiducial EoR levels are expected to be roughly 10^{-5} times the peak cross-correlation foreground power in the visibility at $k_{\parallel} \sim 0.1 \ h \, {\rm Mpc}^{-1}$, and is generally thought to be even weaker at higher k_{\parallel} (Mesinger et al. 2011). If reflection systematics have inherent amplitudes of around 10^{-3} , then a few orders of magnitude of further suppression will push them below expected EoR levels at low k. In practice, nonideal effects like frequency evolution of the reflection parameters will limit the precision of reflection calibration, which has been observed in real instruments (Ewall-Wice et al. 2016). Indeed, inclusion of such effects in our systematic simulation will likely degrade our algorithm performance. However, if frequency evolution is a limiting factor for reflection calibration, one simple strategy is to split the full bandwidth into multiple subbands and perform reflection calibration independently on each of them, with the caveat that non-negligible frequency evolution within each subband may need to be mitigated in other ways. One can also do this more self-consistently by estimating the reflection parameters and their frequency dependence across the full band, however, we defer this to future work.

3.2. Modeling Cross Coupling

Antenna cross-coupling systematics are a baseline-dependent effect and as such must be modeled and subtracted for each cross-correlation visibility independently. In other works, cross coupling has been modeled as a phase-stable term in the data that can be removed by applying a finite-impulse response (FIR) high-pass filter to the data (Parsons et al. 2010; Ali et al. 2015; M. Kolopanis et al. 2019, in preparation). The algorithm described in this work is conceptually quite similar in that we

take advantage of cross-coupling's slow time variability to model it, but is different in its methodology. A comparison of cross-coupling subtraction techniques is done in Appendix B. Note that the method presented here does not assume that the instrumental bandpass has been calibrated out: these two steps are in principle interchangeable. In practice, it helps if at least the antenna cable delays are calibrated out such that the main foreground lobe shows up at the expected delays of $\tau\approx 0\,\mathrm{ns}$, but again this is not strictly necessary.

Our semiempirical approach starts with the cross-correlation visibility Fourier transformed across frequency, \widetilde{V}_{12} , such that it is in the time and delay domain. If we think of the visibility as a 2D rectangular matrix, we can use singular value decomposition (SVD) to decompose the matrix as

$$\widetilde{V} = TSD^{\dagger}, \tag{14}$$

where T is a unitary matrix containing basis vectors (also referred to as eigenmodes) across time, D is a unitary matrix containing basis vectors across delay, and S is a diagonal matrix containing the weight (or their singular values) of each mode in the data. There may be components of our data matrix, \widetilde{V} , that are inherently low rank, like a slowly time-variable systematic for example. Thermal noise in the visibility, on the other hand, occupies the full rank of the data matrix. SVD can help us model and pull out the low-rank components of the matrix, thus providing an approach for systematic removal on a per-baseline basis.

Our SVD-based systematic removal algorithm operating on an individual visibility takes the following steps:

- 1. Fourier transform the visibility waterfall to delay space.
- 2. Apply a rectangular band-stop window across delay to down-weight foregrounds at low delays.
- 3. Decompose the visibility via SVD.
- 4. Choose the first *N* modes to describe the systematic and truncate the rest.
- 5. Take the outer product of the remaining *T* and *D* modes to form *N* data-shaped templates.
- 6. Multiply each template with their corresponding singular value in *S* and sum them to generate the full-time and delay-dependent systematic model.
- 7. Fourier transform the systematic model from delay space back to frequency space and subtract it from the data.

A demonstration of this process on simulated visibilities is shown in Figure 4. In this example, the simulation contains foregrounds and cross-coupling systematics, but is free of both thermal noise and EoR components. We start with a simulated visibility spanning roughly 9 hr in LST with 1000 time bins and spanning a bandwidth from 120-180 MHz with 256 frequency bins. By Fourier transforming it to the delay domain (a), we see that foregrounds are confined to low delays, while crosscoupling systematics span a wide range of delays at positive and negative delay offsets. Applying a band-stop windowing function across the delay before taking the SVD (hatched region) assigns zero weight to delay modes dominated by foreground signal at $|\tau|$ < 300 ns. The result of the SVD shows significant isolation of the information content of the systematic in the visibility into the first eigenmode (c). The first time eigenmode (b) indeed shows it to be slowly time variable, as we would expect for a cross-coupling systematic (see Section 2). The outer product of the first time and delay

eigenmodes multiplied with their singular value yields a systematic template with the shape of our original data matrix (d). Taking this single template as our systematic model (equivalent to setting N=1) and subtracting it from the data yields the systematic-subtracted data (f).

We see in (d) that a cross-coupling model with N=1 provides good subtraction of the systematic, but is not enough to completely remove it: based on Figure 4 (c) we can see that it provides effectively three orders of magnitude of suppression, which, depending on the inherent amplitude of the systematic, may or may not be enough to push it below fiducial EoR levels. We can remove more and more of the systematic by increasing the number of SVD modes we incorporate into the systematic model. However, as is the case with empirically based models, this has the side effect of possibly introducing structure from other components of the visibility that we do not want in our systematic model, such as the EoR itself. If the EoR signal was somehow soaked up by our systematic model, then by subtracting the model from the data we are inducing EoR signal loss, which is highly undesirable.

To limit EoR signal loss in the process of systematic subtraction, we can filter the systematic model to reject Fourier modes that we know hold EoR power. In general, if a signal occupies the visibility in the fringe-rate domain with variance given by $\sigma(f)^2$ and we enact a filter on it by multiplying by a weighting function w(f), then the total power of the signal before filtering, P_{before} , can be related to the total power after filtering, P_{after} , as

$$\frac{P_{\text{before}}}{P_{\text{after}}} = \frac{\int df \ \sigma(f)^2}{\int df \ \sigma(f)^2 w(f)^2}.$$
 (15)

Therefore, if we know statistically how the EoR will populate the visibilities in the fringe-rate domain—in a sense deriving their power spectral density functions (PSDs)—we can construct a Fourier filter that is tailored to reject Fourier modes in the systematic model that we know hold EoR power.

This is closely related to the optimal fringe-rate formalism outlined in Parsons et al. (2016). In Figure 5 we show peaknormalized PSDs of an EoR sky model at 120 MHz for various baselines in the array, which describe the relative amount of signal power occupied by different fringe rates. We derive these via ensemble simulations of the same EoR sky while varying the initial seed (Appendix A). The PSD of a simulated HERA cross-coupling systematic is also plotted (black-dashed curve). While centered at a fringe rate of 0 mHz, the systematic has a tail that extends out to negative and positive fringe rates, the latter being where most of the power from the EoR also lies. Conversely, while most of the EoR power lies at positive fringe rates for many baselines, some of its power also extends to zero and negative fringe rates. Baselines that are longer along the east-west direction have more EoR power pushed to higher fringe rates and thus are more naturally separated from crosscoupling systematics, while baselines that are purely northsouth in orientation see an EoR signal that is centered at $f \sim 0$ mHz, and almost completely overlaps the cross-coupling systematic.

Each curve in Figure 5 integrated out to 99% of their total area yields the domain in fringe-rate space where 99% of the EoR power is contained in the visibility. We tabulate these bounds in Table 1 for a few HERA baselines at $\nu=120$ MHz. If we low-pass filter any of the visibilities in Figure 5 in

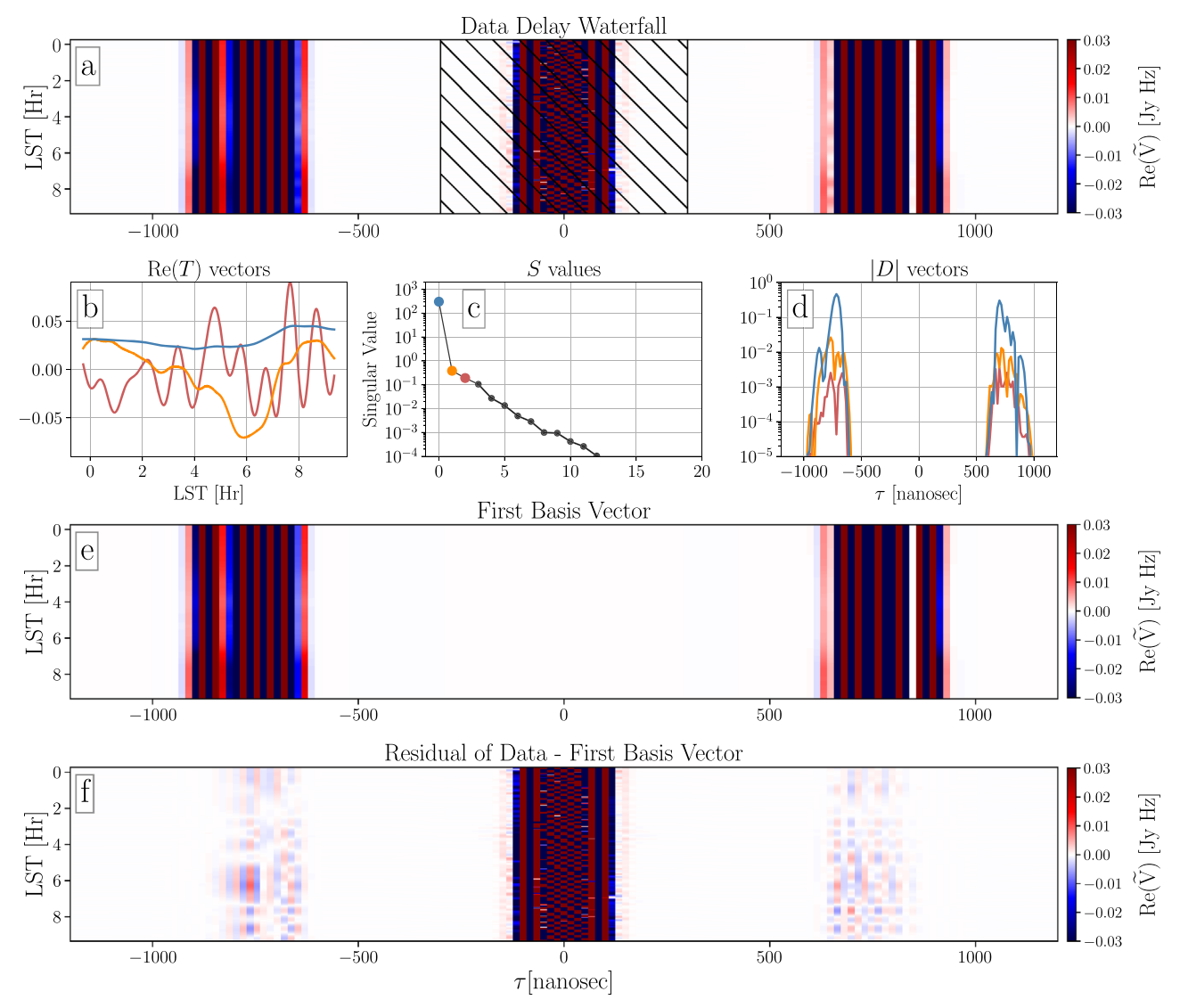


Figure 4. Semiempirical modeling and removal of cross-coupling systematics from a simulated cross-correlation visibility. (a) A simulated visibility with foregrounds (center) and cross-coupling systematics (left and right). The hatched region of $|\tau| < 300$ ns is assigned zero weight before taking the SVD. (b)–(d) The resulting T modes, singular values, and D modes after factorization via SVD. The D modes are artificially offset for visual clarity. (e) The outer product of the first T and T mode multiplied with its singular value yields the first basis vector having the shape of the original data matrix. (f) The difference of the systematic model and the original data shows decent subtraction of the systematic, but is not enough to completely remove it from the data.

fringe-rate space by applying a symmetric top-hat filter with a maximum extent $f_{\rm max}$ given by these lower bounds, then Equation (15) tells us we will retain 99% of the EoR power in the data after filtering, which for our purposes is an effectively lossless operation given other more dominant sources of error. This result means that our ability to safely remove cross-coupling systematics is baseline-dependent: for baselines with large east—west lengths (e.g., blue curve), we can filter out the vast majority of the systematic without attenuating the EoR. For shorter baselines (e.g., green curve), we may only be able to remove part of the systematic, and for baselines oriented along the north—south direction (e.g., red), we may not be able to remove any cross-coupling systematics, if they exist.

Armed with the ability to filter an arbitrary signal without attenuating its EoR component, we can return to the problem of choosing the appropriate number of eigenmodes to use in describing a cross-coupling systematic in the data. We noted in Figure 4 that by increasing the number of SVD eigenmodes used to describe our systematic model, we might be able to

remove more of the systematic from the data. Figure 6 proves this on a simulated visibility, now simulated with an EoR and foreground component (green curve) corrupted by a crosscoupling systematic at high delays (blue curve). We also show SVD-based systematic removal with increasingly more eigenmodes used to describe the systematic (orange curve). We can see that going from N = 1 (a) to N = 5 (b) enables us to subtract more of the systematic from the data. However, at some point we expect low-level eigenmodes to be influenced by other components of the data, such as EoR, foregrounds, or noise, which raises the possibility of removing those components along with the systematic. This is shown in (c), where with N = 15 we have over subtracted the systematic and caused signal loss of EoR power at high delays. One might conclude from this that N = 5 is the "sweet spot" choice for the number of eigenmodes to use, but this choice is conditional on the relative amplitude between EoR and systematic: without knowing the amplitude of EoR in the data a priori, we have no way of knowing the appropriate number of eigenmodes to use

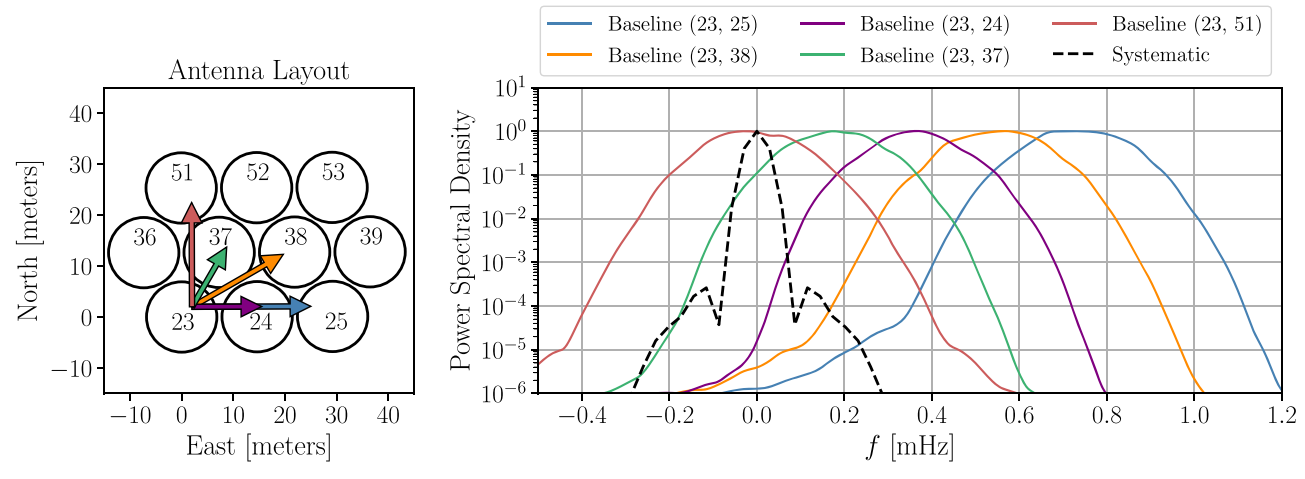


Figure 5. Peak-normalized PSDs in fringe-rate space of an uncorrelated Gaussian EoR sky model for HERA baselines at 120 MHz. Left: a subset of the HERA array showing its shortest baselines arranged in a hexagonal pattern. The arrows denote four unique baseline orientations. Right: peak-normalized PSDs describing how an EoR sky signal populates the inteferometric visibility in the fringe-rate domain, as well as a cross-coupling systematic (black-dashed curve).

Table 1EoR Visibility Power Bounds

Baseline Length	Baseline Angle	99% Power Bounds
29.2 m	0°	0.46 < f < 0.95 mHz
25.3 m	30°	0.31 < f < 0.77 mHz
14.6 m	0°	0.14 < f < 0.58 mHz
14.6 m	60°	-0.05 < f < 0.40 mHz
25.3 m	90°	-0.27 < f < 0.21 mHz

Note. Power bounds are defined at $\nu=120$ MHz. Baseline angle is defined in east north up coordinates as ϕ° north of east (e.g., left of Figure 5).

that would enable us to subtract the systematic without attenuating EoR. This makes the algorithm as originally described in effect unusable, because it is an operation that is dangerously lossy to EoR signal.

The solution to this problem is to apply a low-pass time filter to the systematic model that is tailored to reject fringe-rate modes occupied by the EoR. Specifically, we can apply a filter to the systematic model T matrix that only keeps structure below some predefined maximum fringe rate, $f_{\rm max}$, such that in the process of subtracting it from the data, all fringe rates $|f| > |f_{\text{max}}|$ are left unaffected. For example, if we could tolerate a maximum of 1% attenuation of EoR power in the process of systematic removal, then f_{max} would be set at the lower bounds tabulated in Table 1. The result of applying such a filter to the SVD eigenmodes is demonstrated in Figure 6(d), which shows the systematicsubtracted data with N = 15 having first applied a low-pass filter to T. Although a significant amount of systematic remains, we can now be confident that we have not attenuated the EoR signal in the data, even while using a large number of eigenmodes to describe the systematic.

In this section we have argued and shown via sky and instrument simulations that we can construct a cross-coupling model that removes the vast majority of the systematic while remaining lossless to the EoR signal (for certain baseline orientations). In real data, however, the fidelity of this model will be fundamentally limited by the thermal noise floor of the observation, as is the case for any signal term modeled on a per-baseline basis. If the cross-coupling systematic is truly baseline-dependent and is uncorrelated between baselines, then

the residual systematic term will integrate down like thermal noise when we combine visibilities and we would not expect it to re-appear in the integrated power spectra. In HERA, for example, there is evidence that the observed cross-coupling systematics are at least partially uncorrelated between baselines (Kern et al. 2019).

4. Signal Loss

We have thus far presented an overview of instrumental systematics that can hinder if not prohibit the detection of the EoR for current and future 21 cm intensity mapping surveys, and have outlined algorithms for modeling and removing them from the data. However, any experiment that wishes to use a systematic removal technique on the data must show that the subtraction did not attenuate the desired signal in the data. In other words, one must quantify and account for possible sources of signal loss in a data reduction pipeline. In this work, we use signal loss to refer specifically to the inadvertent subtraction of sky signal (EoR or foreground) from the visibilities.

Quantifying signal loss can be done in a variety of ways, depending on the nature of the algorithm one wants to test (Cheng et al. 2018; Mouri Sardarabadi & Koopmans 2019). In general, however, we can quantify the amount of signal loss induced by an algorithm by generating two identical mock data sets, introducing a systematic to one of them, attempting to remove it, and then comparing the end result power between the two data sets. For this analysis, we generate mock observations using the same simulations used in Section 3, but now in addition to diffuse foregrounds and systematics we introduce an EoR component. The EoR sky model is an uncorrelated Gaussian random field across both the spatial and frequency axes with a variance of 25 mK² (see Appendix A for details).

We simulate the EoR and foreground visibilities separately, and then assign their sum as V_1 . Next we create and add in a systematic visibility and assign their sum as V_2 . Lastly, we create a visibility model of the systematic using our algorithms presented above, remove it from the data and assign the

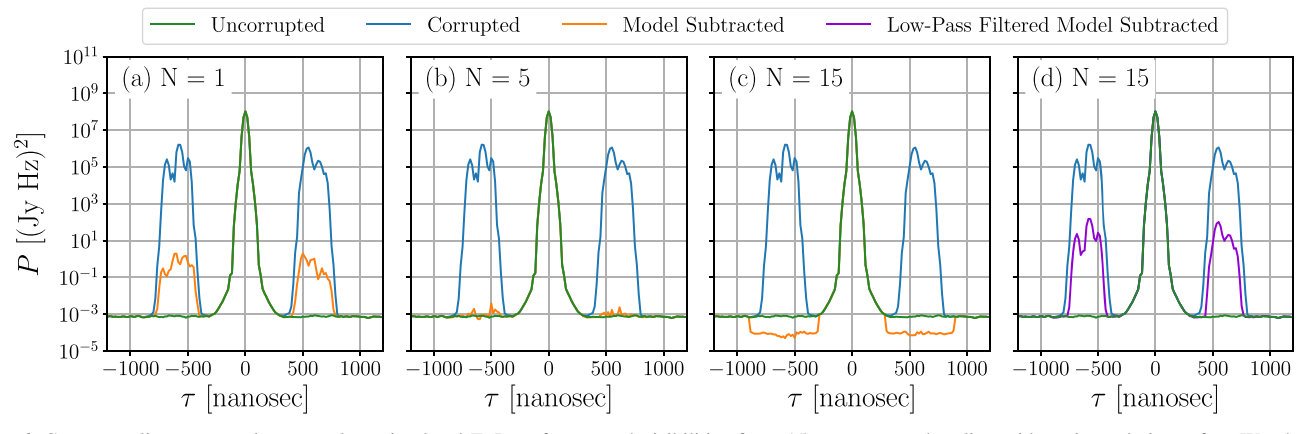


Figure 6. Cross-coupling systematic removal on simulated EoR + foreground visibilities for a 15 m east-west baseline with various choices of N. We show the visibility amplitude averaged over LST for the uncorrupted data (green curve), the data corrupted by a cross-coupling systematic (blue curve) and the systematic-model-subtracted data (orange curve) for N = 1, 5, and 15 (a, b, and c respectively). In the last panel, we show the result of low-pass filtering the SVD T modes before forming the full systematic model and subtracting it from the data. For the baseline at hand, we do this with a fringe-rate cutoff of $f_{\text{max}} = 0.14$ mHz (Table 1). This shows that by low-pass filtering the systematic model, we can constrain it such that it removes the systematic as much as possible while not attenuating the EoR, and is therefore optimal even if it leaves some of the systematic in the data.

residual as V_3 , which can be summarized as follows:

$$V_1 = V_{\text{eor}} + V_{\text{fg}}$$

 $V_2 = V_1 + V_{\text{sys}}$
 $V_3 = F(V_2) = V_2 - V_{\text{mod}},$ (16)

where F is a systematic removal algorithm whose signal loss properties we would like to quantify, and whose effect is to subtract a model of the systematic, $V_{\rm mod}$, from the corrupted visibility. Note we do not include a thermal noise term, which is done so that we can probe the signal loss properties of the algorithms down to the extremely weak levels of a fiducial EoR signal.

Each visibility has an associated total power, which is a real-valued quantity and can be calculated as the square of the Fourier transformed visibility. In the ideal EoR + foreground case, this is

$$P_1 = \widetilde{V}_1 \widetilde{V}_1^* = P_{\text{eor}} + P_{\text{fg}} + 2 \operatorname{Re}(P_{\text{eor,fg}}), \tag{17}$$

where \widetilde{V} signifies the visibility Fourier transformed from frequency to delay space, and $P_{\text{eor,fg}}$ represents the cross-power between $\widetilde{V}_{\text{eor}}$ and $\widetilde{V}_{\text{fg}}$. Similarly, we can write the power of the systematic-subtracted visibility as

$$P_{3} = \widetilde{V}_{3}\widetilde{V}_{3}^{*} = P_{\text{eor}} + P_{\text{fg}} + 2 \operatorname{Re}(P_{\text{eor,fg}}) + P_{\text{sys}} + P_{\text{mod}} - 2 \operatorname{Re}(P_{\text{sys,mod}}) + 2 \operatorname{Re}(P_{\text{eor,sys}}) - 2 \operatorname{Re}(P_{\text{eor,mod}}) + 2 \operatorname{Re}(P_{\text{fg,sys}}) - 2 \operatorname{Re}(P_{\text{fg,mod}}).$$
(18)

In the case where we have *perfectly subtracted* the systematic from the visibility (i.e., $V_{\rm mod} = V_{\rm sys}$), we see that the systematic power terms cancel with the model power terms such that, not surprisingly, we get that $P_3 = P_1$. In the case where we have *imperfectly subtracted* the systematic—either by incorrect estimation of its phase and/or amplitude—the cross terms no longer cancel. What this means for the total power of the resultant visibility, P_3 , depends on how well matched the model visibility is to the systematic, in addition to the relative inherent amplitude of the sky signal versus the systematic. For example, in the case of

an imperfect systematic model, then we can see that this will always be true: $P_{\rm sys} + P_{\rm mod} > 2\,{\rm Re}(P_{\rm sys,mod})$, meaning their difference results in excess power. Whether or not the EoR and foreground cross term residuals in Equation (18) result in overall positive or negative power depends on how well matched the systematic model is to either EoR or foregrounds.

Given this, we can construct a simple metric,

$$R_3(\tau) = \frac{\langle P_3(\tau) \rangle}{\langle P_1(\tau) \rangle},\tag{19}$$

to determine whether or not a step in our data analysis induces signal loss. Here the $\langle \rangle$ denotes an ensemble average over many realizations of the visibilities with the same kind of sky signal and systematic. Taking the ensemble average before taking the ratio is done to ensure the power spectra are properly normalized. Signal loss occurs anytime $R_3(\tau) < 1$, meaning that our model-subtracted visibility, V_3 , has less power in it than our uncorrupted visibility, V_1 . Specifically, EoR signal loss occurs anytime $R_3(\tau) < 1$ at delays we know to be dominated by EoR over foregrounds, such as all delays significantly outside the geometric delay of the baseline. In the case of $R_3(\tau) > 1$, the resultant visibility is systematic limited, but importantly, is not underreporting the power in the data relative to the pure sky signal visibility. We can also form the metric $R_2(\tau)$ using P_2 instead of P_3 , which informs us of the relative amplitude of the raw systematic (without any removal) compared to the underlying sky signals.

Whether or not an algorithm is lossy in practice can depend on the relative amplitude between the signal and systematic present in the data. As such, we need to compute the *R* metric while varying the relative amplitude between the EoR and systematics. Cheng et al. (2018), for example, do this by repeatedly injecting mock EoR signals into their analysis pipeline with increasing amplitude. In this study we take the opposite approach. We adopt a fixed EoR amplitude consistent with rough theoretical expectations and insert systematics at amplitudes below, equal to, and above the adopted EoR amplitude and compute *R*. This approach is more consistent with what we expect to find in the real data: at certain times, frequencies, or baselines, we may find systematics to be heavily

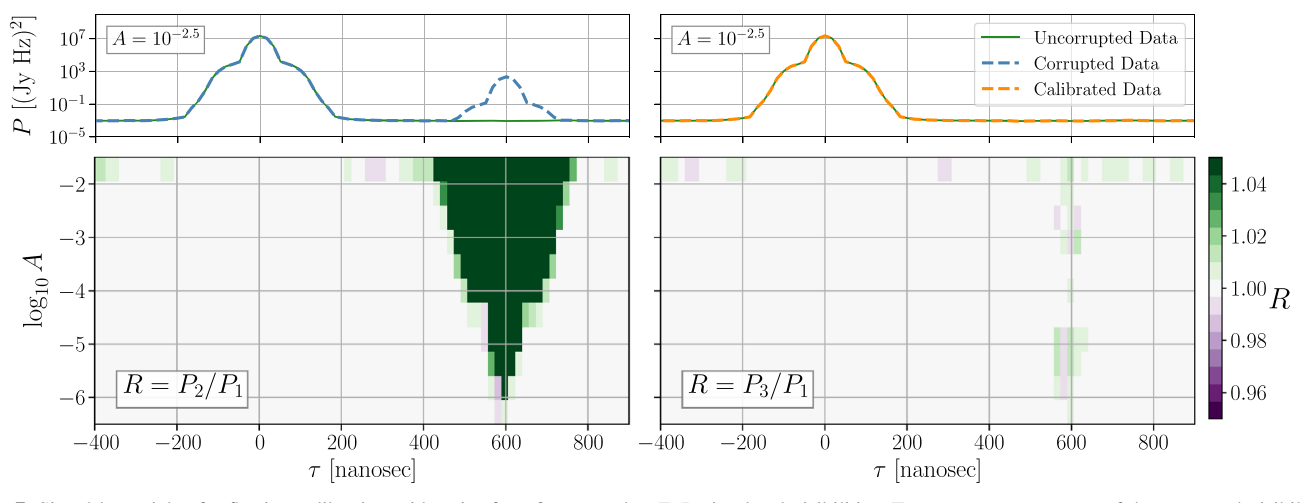


Figure 7. Signal loss trials of reflection calibration with noise-free, foreground + EoR simulated visibilities. Top row: power spectra of the corrupted visibility V_2 (blue-dashed curve), the uncorrupted visibility V_1 (green-solid region) and the calibrated visibility V_3 (orange-dashed line) from a signal loss trial with a reflection amplitude of $A = 10^{-2.5}$. Bottom row: heatmaps of the signal loss R metric computed for the corrupted data (left) and the calibrated data (right) as a function of reflection amplitude (y-axis) and delay (x-axis). The residual fluctuation about R = 1 in the right panel is encompassed within the $1/\sqrt{N}$ sample variance of our finite ensemble average.

dominant, while at other times, frequencies, or baselines, there may be no systematics at all.

4.1. Signal Loss in Reflection Calibration

To test signal loss in the context of reflection calibration, we precompute the visibilities for a single diffuse foreground model and 100 independent EoR models, with each simulation spanning 8 hr of LST and 1000 individual time integrations. Because HERA has a beam crossing time of about 1 hr, this yields an effective number of independent foreground + EoR simulations of ${\sim}800$. The adopted EoR model is an uncorrelated Gaussian field across angular position and frequency with a variance of $25\,\mathrm{mK}^2$ (Appendix A).

A single signal loss trial takes the following steps. First we choose a random EoR model from our library of precomputed visibilities and add it to our foreground visibility (V_1) . We then make a copy of it and insert a reflection with a delay of 600 ns, a random phase, and a single amplitude across frequency using Equation (4) (V_2) . We then model the reflection in the simulated autocorrelation knowing only the approximate delay range at which it appears, and then apply the derived gain solution to the cross-correlation visibilities (V_3) . Next we compute power spectra of each data product $(P_1, P_2, \text{ and } P_3)$. We then repeat this on the order of 100 times, each with a different random EoR model, and then take their average to approximate the ensemble average in Equation (19). We then form the R_2 and R_3 metrics as a function of time and delay, i.e., $R_3(t, \tau)$, and average over time to collapse them onto a single axis across delay. This entire procedure produces one signal loss trial, which is defined uniquely by the amplitude, A, of the reflection inserted into the visibility.

Figure 7 shows multiple trials for different reflection amplitudes in the range of 10^{-6} – 10^{-1} . The top row shows power spectra of each of the three visibility products as a function of delay for one trial when $A = 10^{-2.5}$. Recall that the reflection amplitude is defined with respect to the visibility, meaning that the observed reflection amplitude in the power spectrum is A^2 . The bottom row shows a heatmap of the signal loss R metric as a function of delay (x-axis) and each trial's reflection amplitude (y-axis). The left panels shows R_2 and the right panel shows R_3 , highlighting the

amount of delay space that is brought down to $R \sim 1$ after reflection calibration, with negligible amounts of signal loss (purple-shaded regions). Furthermore, the weak levels of fluctuating residual systematic and signal loss observed at the $\sim\!2\%$ level are within the $1/\sqrt{N}$ sample variance of our finite ensemble average. For context, HERA cable reflection amplitudes are seen at around 10^{-3} (Kern et al. 2019).

4.1.1. Multi-reflection Regime

Above we probed for signal loss when performing reflection calibration on a single reflection that was isolated in delay space. Next, we relax this assumption and test how the the algorithm performance and signal loss properties change when we add in more reflections, which is relevant for any instrument with multiple cables, or with cables that have sub-reflections along the length of the cable (Ewall-Wice et al. 2016; Kern et al. 2019). We choose to model the relative amplitude of these reflections as an inverse power law as a function of delay with a nominal reflection amplitude of $A = 3 \times 10^3$. Our algorithm models and calibrates out each reflection one at a time, starting with the reflection with the largest amplitude. We do not feed the algorithm the position of each reflection (it searches for it automatically within a specified range of delays), but we do assume we know the number of reflection inherent in the data, which controls how many times we iterate the algorithm.

Our first test shown in Figure 8 involves only five reflections inserted across a relatively wide region in delay, such that they can be considered nonoverlapping (or unconfused). In the top panels, we show power spectra of the uncorrupted data (P_3 ; green), the corrupted data (P_2 ; blue line) and the reflection calibrated data (P_3 ; orange-dashed line), along with a line marking the EoR amplitude in the data (gray). We show this for the autocorrelation visibility (left) and a 29 m cross-correlation visibility (right). In the bottom panels we show the signal loss metrics R_2 (blue) and R_3 (orange-dashed line). Recall that reflection calibration builds up a set of gains strictly from the autocorrelation, and then applies those gains to the cross correlations. We find that our algorithm performs exceptionally well in this regime: removing reflections down to the inherent

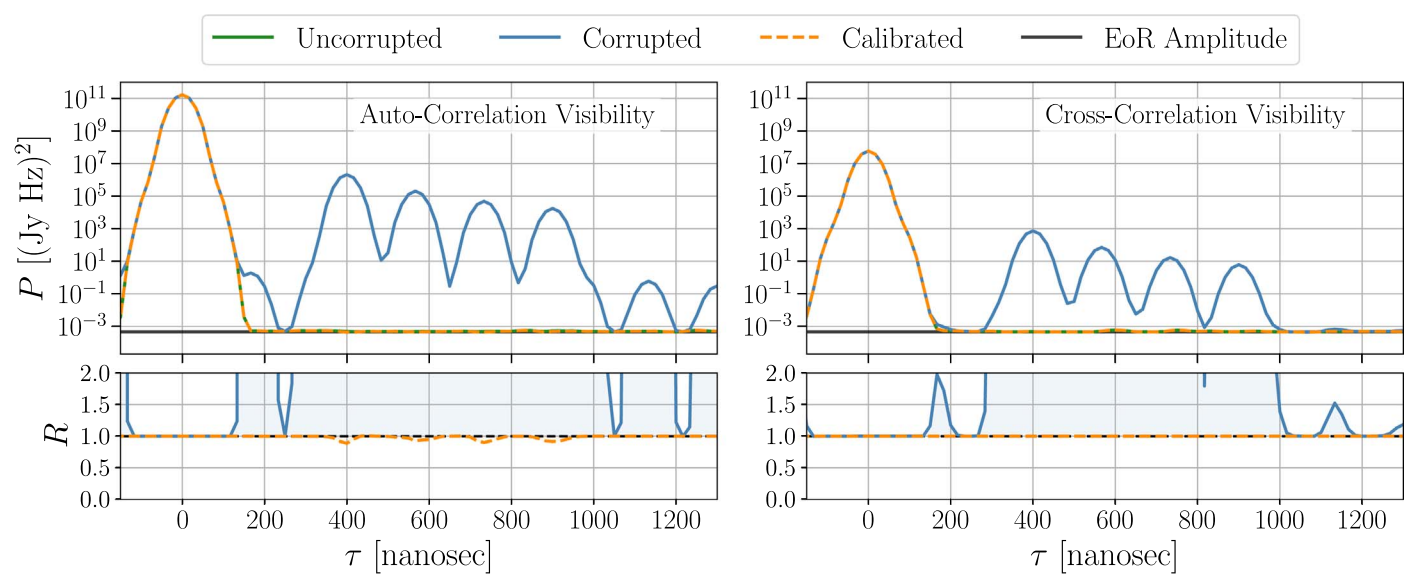


Figure 8. Reflection calibration run on an autocorrelation (left) in a low-confusion, multi-reflection regime, where we then apply the resultant gains to a cross-correlation visibility with a 29 m baseline length (right) and repeat a few dozen times. In the top panels, the (ensemble average) power spectrum of the uncorrupted data (P_1 ; green), corrupted data (P_2 ; blue curve) and calibrated data (P_3 ; orange-dashed curve) are plotted along with a line denoting the underlying EoR amplitude in the data (gray). Signal loss metrics R_2 (blue curve) and R_3 (orange curve are shown in the bottom panels. We see that while reflection calibration can lead to a slight amount of signal loss at the reflection delays of the autocorrelation visibility (bottom-left, dashed line), signal loss is not observed to an appreciable degree in the cross-correlation visibility (bottom-right, dashed line).

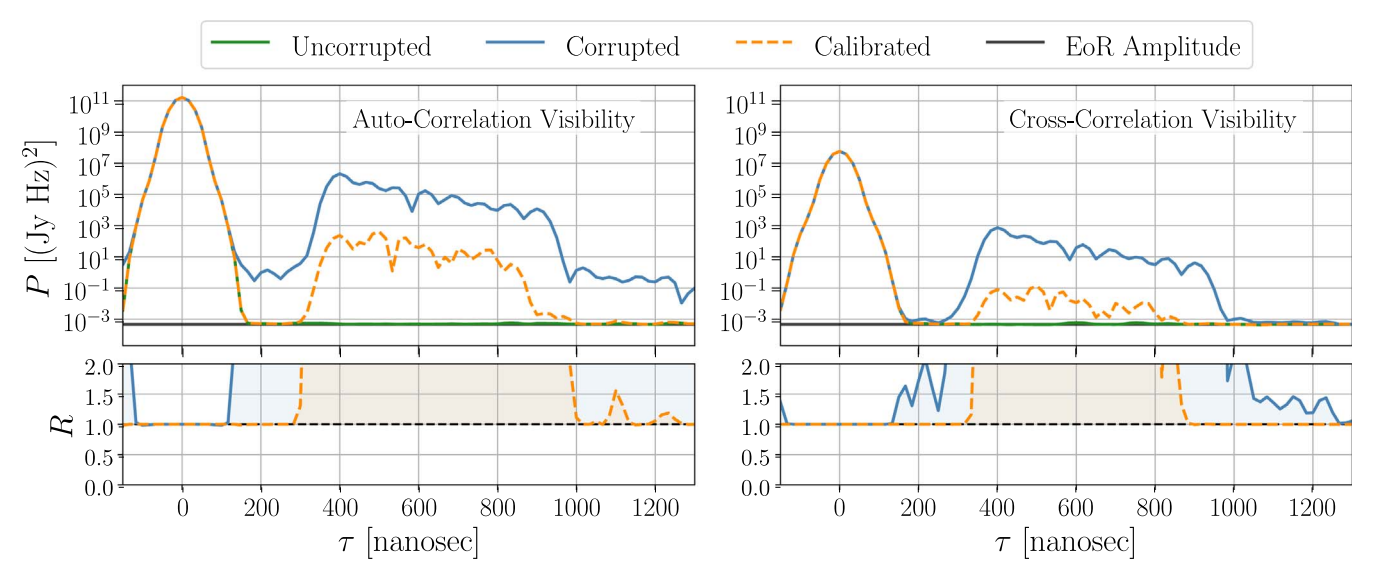


Figure 9. Same figure as Figure 8 but now in a higher-confusion, multi-reflection regime. Importantly, even when reflection calibration encounters confusion in its peak finding algorithm and fails to perfectly model the reflection, it still does not induce appreciable signal loss in the cross-correlation visibility (bottom-right, orange).

sidelobe floor of the autocorrelation, which is more than enough to bring the systematics to the EoR level in the crosscorrelation visibility. We find that while reflection calibration can lead to slight signal loss in the autocorrelation visibility, we find no appreciable levels of signal loss in the cross correlation.

Our next test shown in Figure 9 increases the number of reflection modes inserted into the same region, such that they become almost entirely overlapping. In this case we can see that our algorithm fails to perfectly calibrate out the reflections in both the autocorrelation (left) and cross correlation (right) due to the partial confusion. Nonetheless, we still find that while imperfect reflection calibration can lead to slight signal loss in the autocorrelation, the cross correlation is resistant to

signal loss. Reflection calibration's resistance to signal loss in the cross correlations is perhaps not surprising, given that reflection calibration operates in an antenna-based space, while EoR and other sky signals live in a baseline-based space. Furthermore, our algorithm solely uses the autocorrelations to estimate the reflection parameters.

In total, our findings suggest that (1) our reflection calibration algorithm performs moderately well even in the many-reflection regime, and that (2) even if a broad delay region is contaminated by reflections, we can still in principle use this region for EoR measurements (or upper limits in the case of imperfect systematic removal) after reflection calibration because it does not suffer appreciable levels of signal loss.

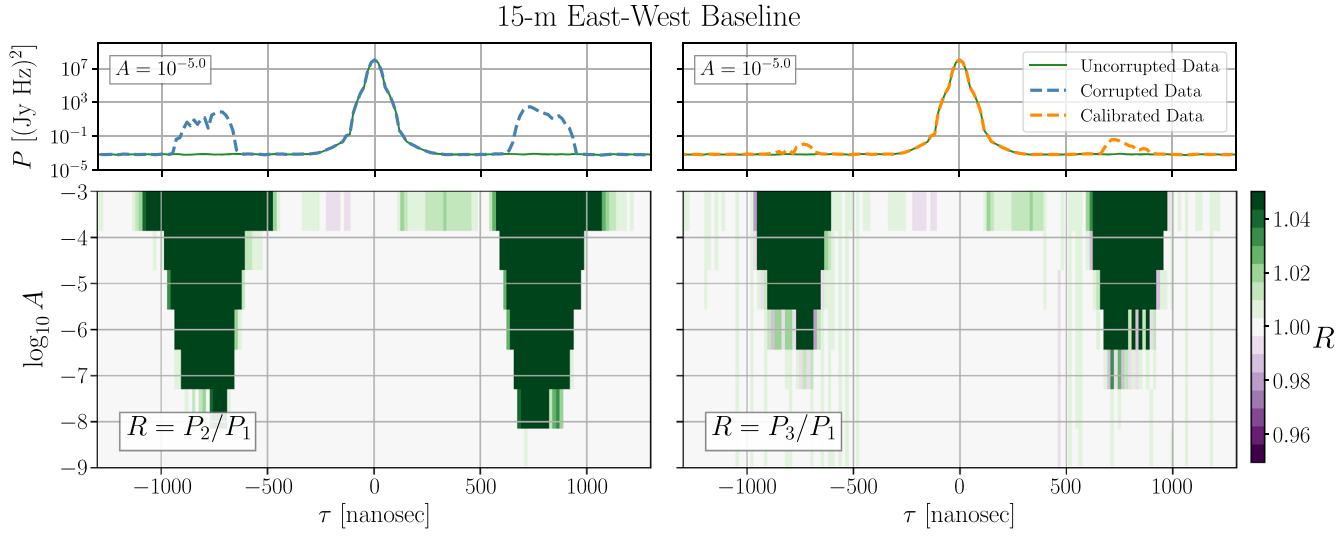


Figure 10. Signal loss trials of cross-coupling removal with noise-free, foreground + EoR simulated visibilities for a 15 m east—west HERA baseline. The systematic model is formed using 20 SVD modes and applies a low-pass time filter with an $f_{\text{max}} = 0.14$ mHz. Top row: power spectra of the corrupted visibility P_2 (blue-dashed curve), the uncorrupted visibility P_1 (green-solid region) and the systematic model-subtracted visibility P_3 (orange-dashed curve) from a signal loss trial with a coupling amplitude $A = 10^{-4}$. Bottom row: signal loss R metric computed for the corrupted visibility (left) and the model-subtracted visibility (right) as a function of coupling amplitude (y-axis) and delay (x-axis), with the model-subtracted visibility (right). No appreciable amounts of signal loss is observed, and the model-subtracted data show roughly four orders of systematic suppression in the power spectrum.

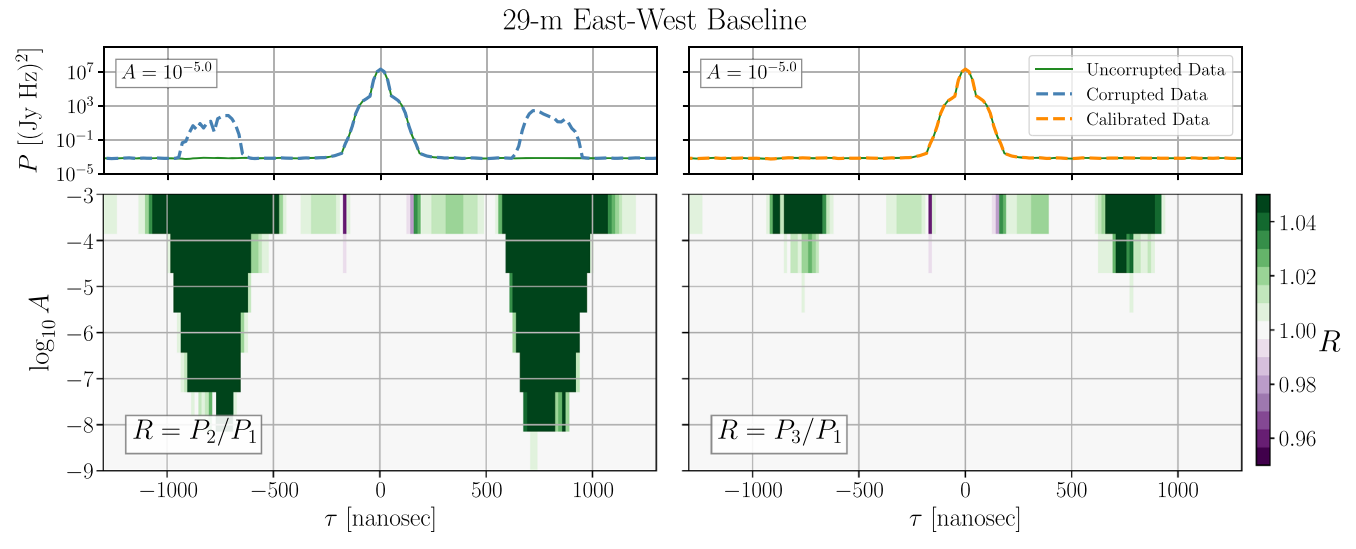


Figure 11. The same signal loss trials for removal of a cross-coupling systematic as described in Figure 10, but for a 29 m east—west baseline using a low-pass time filter with $f_{\text{max}} = 0.46$ mHz. In this case we get upwards of six orders of magnitude in systematic suppression in the power spectrum.

4.2. Signal Loss in Cross-coupling Subtraction

In this section, we quantify signal loss for cross-coupling subtraction in a similar manner. Based on our conclusions from Section 3.2, we expect our cross-coupling subtraction to be effectively lossless to EoR by construction, but testing this against ensemble signal loss trials is a good double-check and validation of our arguments. The rough functional form of the simulated cross coupling inserted into the visibilities is informed by cross-coupling systematics observed in the HERA Phase I system (Kern et al. 2019). The simulations used are fundamentally the same as those used in Section 4.1, except simulated with cross-coupling systematics rather than cable reflections. To simulate cross coupling in a cross-correlation visibility, we use Equation (12) to insert \sim 25 modes spanning $700 < |\tau| < 900$ ns with a decaying power law as a function of $|\tau|$ for their relative amplitudes,

normalized such that the maximum amplitude relative to the peak *autocorrelation* foreground power equals a predefined amplitude, A. In the process of systematic removal, we model the systematic with N=20 SVD eigenmodes and apply a low-pass fringe-rate filter on the SVD T modes using a Gaussian process (GP) smoothing (see Appendix B) with a maximum fringe rate given by the lower bound in Table 1. We then Fourier transform the data from frequency to delay space using a seven-term Blackman–Harris window, and average across ensemble trials. After forming the R_2 and R_3 metrics as a function of time and delay, we truncate 5% of the time bins on either edge of the time axis before taking their time average to limit the influence of boundary effects in the smoothing process.

The result is shown in Figures 10 and 11, which shows signal loss trials run on a 15 m east—west baseline and a 29 m east—west baseline, respectively. As expected, we see better

systematic suppression for the longer baseline, where the EoR signal is inherently more isolated from the systematic in fringerate space. We also see that in the case of strong coupling amplitudes we cannot completely suppress the systematic down to EoR levels; however, we can nonetheless suppress the systematic by roughly four orders of magnitude in power for the 15 m baseline and eight orders of magnitude in power for the 29 m baseline. Importantly, we show that the algorithm presented does not significantly attenuate EoR in the data, with residual fluctuations about R=1 at the 1% level in power. While this result is not surprising given the fact that in Section 3 we constructed our systematic model to explicitly be lossless to EoR, it is still a useful cross-check on our algorithm and its implementation on the data.

5. Summary

In this work, we present an overview of 21 cm radio survey systematics related to internal instrument coupling, including signal chain reflections and antenna cross couplings. Such systematics will hinder cosmological surveys aiming to detect and characterize the 21 cm signal from the EoR and Cosmic Dawn. We study the temporal and spectral behavior of these systematics in simulations, and propose techniques for modeling and removing them from the data without attenuating the desired cosmological signal. We further test the signal loss properties of these techniques with simulated HERA sky and systematic simulations.

For simulated cable reflection systematics in the absence of noise, our method can estimate its parameters to 1 part in 10⁶ and achieve suppression of over eight orders of magnitude in the power spectrum for both isolated and semi-isolated reflections. In practice, nonideal effects like frequency evolution in the reflection parameters will limit the performance of this technique on real data. Through signal loss trials we show that reflection calibration, when modeled from the autocorrelation visibility, is resistant to EoR signal loss in the cross-correlation visibilities.

Antenna cross couplings are another category of systematics that we address in this work. We present an SVD-based modeling technique that, when low-pass filtered along the time axis, can suppress cross-coupling systematics by four orders of magnitude in the power spectrum for HERA's short east-west baseline, and eight orders of magnitude or more for baselines of longer projected east-west separation in the absence of noise. We show that we can tailor our systematic model to minimize its susceptibility to inducing EoR signal loss, and additionally prove this with signal loss trials. This result has critical implications for enabling 21 cm experiments to mitigate systematics that would otherwise hinder if not prohibit them from making a robust detection of the EoR signal. A companion paper (Kern et al. 2019) applies these methods to HERA Phase I data as a method demonstration, showing we can suppress reflection and cross-coupling systematics down to the array-integrated noise floor of the data for a single nightly observation.

The authors would like to thank Daniel Jacobs, Aaron Ewall-Wice, Miguel Morales, Jonathan Pober, Bryna Hazelton, James Aguirre, and Adrian Liu for helpful discussions related to this work. This material is based upon work supported by the National Science Foundation under Grant Nos. 1636646 and 1836019 and institutional support from the HERA collaboration partners. This research is funded in part by the Gordon and

Betty Moore Foundation. J.S.D. acknowledges the NSF Astronomy and Astrophysics Postdoctoral Fellowship (NSF Award #1701536). A.E.L. would like to acknowledge NASA Grant 80NSSC18K0389.

Appendix A Simulated Visibilities with healvis and hera sim

We use the numerical visibility simulation package healvis⁶ to compute mock observations of foreground and EoR sky models. healvis numerically integrates the measurement equation (Equation (1)) by representing the sky and directiondependent antenna primary beam response as HEALpix maps (Górski et al. 2005), and summing their product with the baseline fringe pattern to compute the visibility. The mechanics of healvis as a simulator is described in more detail in Lanman & Pober (2019). Our simulations use HEALpix sky maps with NSIDE = 128 and use a frequency and angulardependent electromagnetic simulation of the HERA dish and feed primary beam response (Fagnoni et al. 2019). The adopted beam model does not include mutual coupling effects. The beam has been smoothed across frequency to limit excess spectral structure above 250 ns, mimicking an idealized HERA beam response. We simulate visibilities for HERA baselines of various orientations and separations, ranging from 0 m in separation (i.e., the autocorrelation) out to 60 m in separation. The sky resolution provided by a HEALpix NSIDE = 128 map is roughly 10 times smaller than the fringe wavelength of the longest baseline in consideration at the highest simulated frequency of $\nu = 180$ MHz.

Foreground visibilities are simulated with HEALpix maps of the diffuse, low-frequency radio sky from the PyGSM package, which is a repackaging of the original 2008 Global Sky Model (GSM; de Oliveira-Costa et al. 2008). We simulate a bandwidth spanning 120-180 MHz with 256 channels and an LST range of roughly 0–8 hr with a time cadence of 30 s (about 1000 time bins), which corresponds to the transit of the cold part of the radio sky. Figure 12 shows the diffuse radio sky from the GSM, a mock EoR realization, and the adopted antenna primary beam response at $\nu = 120\,\mathrm{MHz}$. The EoR model is constructed as an uncorrelated δT field with a variance of 25 mK², consistent with fiducial expectations for the signal at EoR redshifts (Mesinger et al. 2011). Its Fourier correlations are modeled as a flat spectrum in P(k): while fiducial EoR models tend to favor EoR as a roughly flat spectrum field in $\frac{k^3}{2\pi^2}P(k)$, for the purpose of using these simulations as mock visibilities for validation and testing we require only a semirealistic EoR model, and believe this difference to have negligible impact on our results. The pixel size of an NSIDE 128 map corresponds to a transverse comoving length scale of \sim 70 cMpc at z = 8, which is larger than the size scales where EoR is correlated during the beginning and middle of reionization. The frequency axis is simulated with a channel resolution of 234 kHz, which at redshift z = 8 corresponds to a comoving length scale of \sim 4 cMpc, which is roughly the scale at which our uncorrelated Gaussian field approximation begins to break down. However, we also believe this to have a negligible impact on our performance and signal loss tests: the most sensitive part of our analysis is the computation of the EoR PSD functions (Figure 5) which relies on the time

https://github.com/RadioAstronomySoftwareGroup/healvis

https://github.com/telegraphic/PyGSM

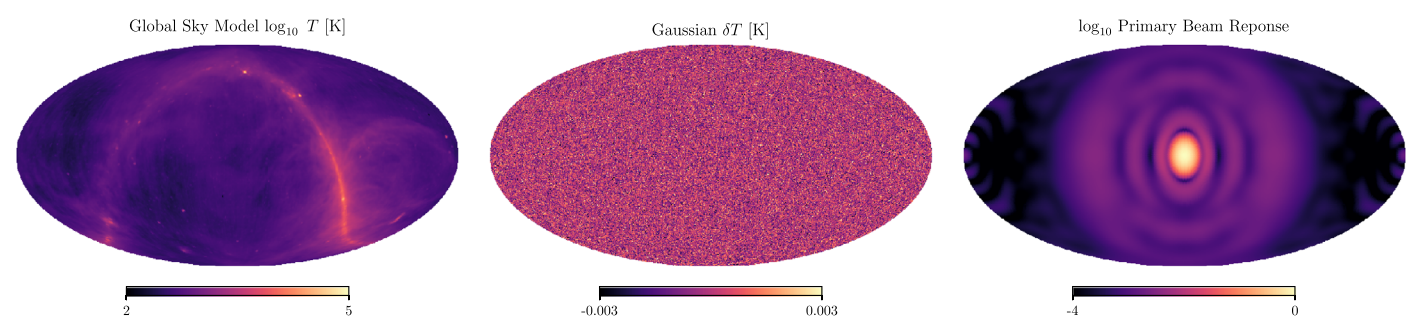


Figure 12. HEALpix sky maps at $\nu = 120$ MHz used for simulating diffuse foregrounds (left) and an uncorrelated EoR field (center). The antenna primary beam response (right) is taken from an electromagnetic simulation of the HERA dish and feed (Fagnoni et al. 2019).

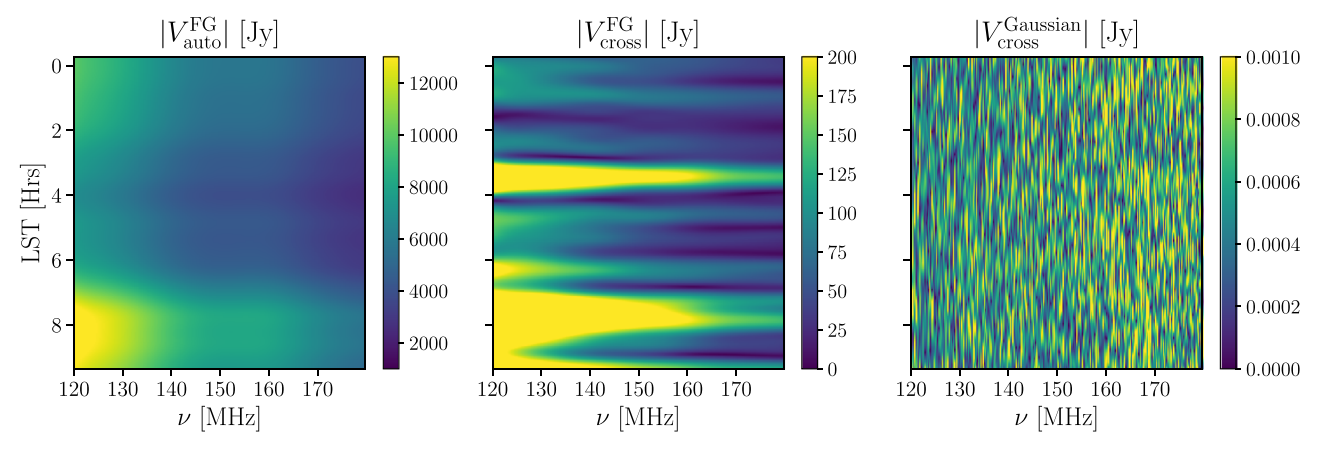


Figure 13. Mock visibilities computed with healvis and hera_sim showing (left) an autocorrelation visibility of diffuse foregrounds, (center) a cross-correlation visibility of diffuse foregrounds, and (right) a cross-correlation visibility of an EoR model.

correlations of the EoR model, not its frequency correlations. Figure 13 shows simulated healvis visibilities of the diffuse foreground (left) and EoR model (center) described above.

We also use the visibility simulation toolbox hera_sim* to model signal chain reflection and cross-coupling systematics. hera_sim is a general purpose toolbox for creating mock observations with realistic instrumental and environmental effects, like thermal noise, reflections and RFI. For inserting systematics into the data, hera_sim uses the equations outlined in Section 2, in particular Equations (5) and (12). For the signal loss trials described in Section 4, we simulate 100 independent EoR visibilities coming from EoR sky maps generated with unique random seeds, and add the GSM foreground visibility to each one. We then add in the relevant systematic to be tested, and use this set of EoR + foreground + systematic visibilities to perform the ensemble average needed for quantifying signal loss.

A.1. EoR PSD Functions for HERA

We use healvis-simulated HERA observations to calculate the expected PSD functions of an EoR-like signal for HERA visibilities. At any given time, a point source locked to the celestial sphere generates a complex sinusoid in the inteferometric visibility with a time period determined by its position on the sky and the fringe profile of the baseline at hand. Over a short time interval, its Fourier transform across time is nearly a delta function at a fringe rate set by the inverse

of its time period. Thus, over short time intervals, points on the sky map to specific fringe rates in the visibility (Parsons et al. 2016), which is also related to the *m*-mode analysis (Shaw et al. 2014). The analytically derived "optimal fringe-rate filter" in Parsons et al. (2016) is a filter that minimizes the noise component of the visibility-based power spectrum error bars, and is related to the PSD of EoR-like signals in the visibility. However, the analytic derivation hinges crucially on the assumption that the beam crossing time is much longer than the fringe-crossing time for a point source on the sky, which was a fairly valid assumption for a wide-field experiment like PAPER. This is not the case for HERA, which has both shorter baselines with wider fringes and also a more compact primary beam. Therefore, calculating the PSD of an EoR-like sky signal is more easily done numerically. We do this by generating over 100 independent EoR sky models with the same variance but different initial seeds. We perform HERA visibility simulations of each sky using healvis, Fourier transform them from LST into the fringe-rate domain, and then take their absolute value and average across each realization. The square of these profiles is shown in Figure 5, which represents a numerically derived PSD of a theoretical EoR-like signal in HERA visibilities. These profiles allow us to tailor visibility Fourier filters to do things like minimize EoR signal loss in systematic subtraction, or to minimize the thermal noise component in the power spectrum error bars. We tabulate the 99% power bounds of these curves in Table 1 for the few baselines presented in this study. We also plot these bounds and provide a fitting formula as a function of projected east-west baseline length in Figure 14, such that one can extrapolate these data points to

⁸ https://github.com/HERA-Team/hera_sim

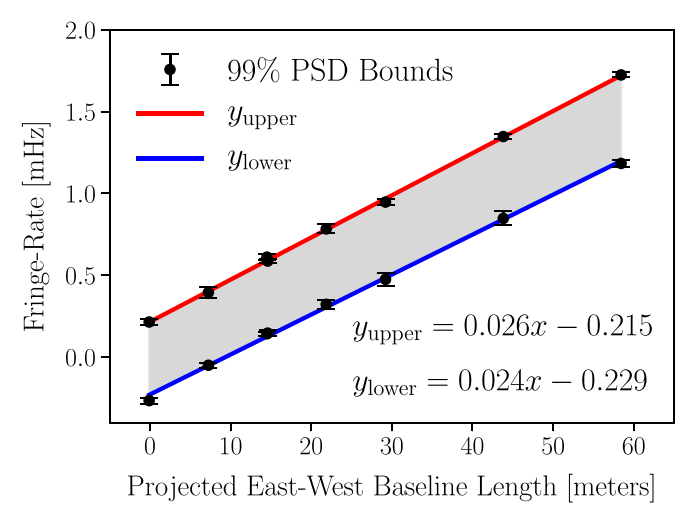


Figure 14. PSD bounds of EoR sky models for HERA baselines in fringe-rate space at $\nu=120$ MHz. The PSD curves are shown in Figure 5, and the bounds quoted correspond to 99% of the total power. Best-fit lines are shown for extrapolation to other HERA baselines.

other baselines in the HERA array. Error bars on the 99% bounds in Figure 14 are calculated via bootstrap resampling over the independent realizations (Efron & Tibshirani 1994).

Appendix B Comparison of Cross-coupling Removal Techniques

In this section, we compare techniques for suppressing slowly fringing systematics (e.g., crosstalk), including the one presented in this work in Section 3. Specifically, we compare the technique from the PAPER Collaboration of convolving an FIR filter in the time domain following the procedures outlined in Parsons et al. (2016), which was applied to PAPER power spectrum analyses for crosstalk suppression (Ali et al. 2015; Cheng et al. 2018; M. Kolopanis et al. 2019, in preparation). In comparing this against the technique from this work, we use two different methods for low-pass filtering the output T modes, the first being a fringe-rate domain deconvolution (DEC), and the second being a Gaussian process regression (GPR) with a fixed-length-scale hyper-parameter. In summary, we find that the SVD-based algorithm with a GPR filtering provides the best systematic suppression outside the foreground wedge. In addition, we find that all algorithms can be tuned to be safe against EoR signal loss in that the structure they subtract from the data can be confined to low-fringe-rate modes where the EoR signal is subdominant.

Filtering visibilities by constructing an FIR filter that zeros out low-fringe rate modes of the data is a technique used by the PAPER Collaboration for suppressing slowly fringing systematics like crosstalk (see Figure 10 of Cheng et al. 2018), and given the convolution theorem, is identical to direct Fourier filtering. In practice, this technique suffers from boundary effects, where because the visibility is not both infinitely sampled and periodic, the systematic subtraction closer to the starting and ending time boundaries is degraded. Another approach is to use a deconvolution in the Fourier domain, which builds a model for the signal by employing the standard CLEAN algorithm (Högbom 1974). By limiting the Fourier modes of the model components to low-fringe-rate modes, one can construct a model that is by construction low-pass filtered. This too suffers from time domain boundary effects, and in

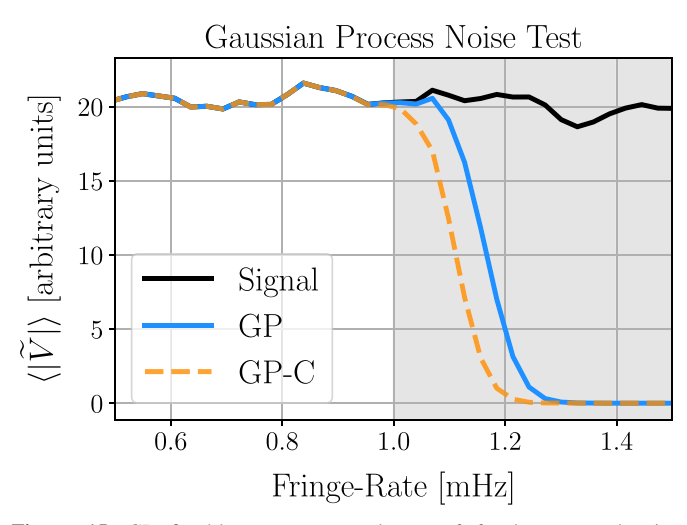


Figure 15. GP fixed-hyper-parameter degree of freedom test, showing simulated noise (black curve), GP smoothing with a squared-exponential kernel and a fixed-length-scale hyper-parameter equivalent to $f_{\rm max}=1.0$ mHz (GP) and constrained-GP smoothing with a fixed-length-scale hyper-parameter equivalent to $f_{\rm max}=0.95$ mHz (GP-C). We can see the former GP model (GP) picks up on signal power slightly outside of the fringe-rate cutoff defined by its length-scale hyper-parameter (shaded region). Degrading this hyper-parameter by 5% makes the model diverge from the signal at the desired fringe-rate cutoff (GP-C).

addition comes with all the subtleties of using the CLEAN algorithm to high dynamic range.

Modeling the time-covariance of the data with a GP eliminates the need to use a Fourier transform, because the modeling is done entirely in the time domain and does not assume exact periodicity of the underlying signal (Rasmussen & Williams 2006); although for our purposes it does assume the signal to be statistically stationary across time. One major concern for a GP-based low-pass filter is the issue of what kinds of time structure it does and does not allow into the model. In other words, we seek to understand its effective degrees of freedom while fitting the data. Without going into too much detail, a GP models the covariance of the data through a kernel function, which sets how correlated two data points are given their distance from each other. For example, a standard squared-exponential kernel describing the covariance between two points in time, t_1 and t_2 , can be written as

$$k(t_1, t_2|\ell) = \exp\left[-\frac{1}{2}(t_1 - t_2)\ell^{-2}(t_1 - t_2)\right],$$
 (20)

where ℓ is a characteristic length scale of correlations and is a hyper-parameter of the kernel. The GP maximum a posteriori function (in addition to its credible intervals) can be calculated, and is generally the desired product of GP modeling (Equation (2.23) of Rasmussen & Williams 2006). By decreasing or increasing the length-scale hyper-parameter, ℓ , we can create GP best-fit functions that have more or less structure in them, respectively.

To use a GP as a low-pass filter, we adopt a squared-exponential kernel with a fixed-length-scale hyper-parameter. If the data is a time series, then this fixed-length scale in time, ℓ , sets the maximum fringe rates allowed by the filter as $f_{\text{max}} = \ell^{-1}$. If we define the effective degrees of freedom of a model as the extent to which it allows power in fringe-rate space, then the effective degrees of freedom of a GP model can be tested via regressing over random noise simulations. We

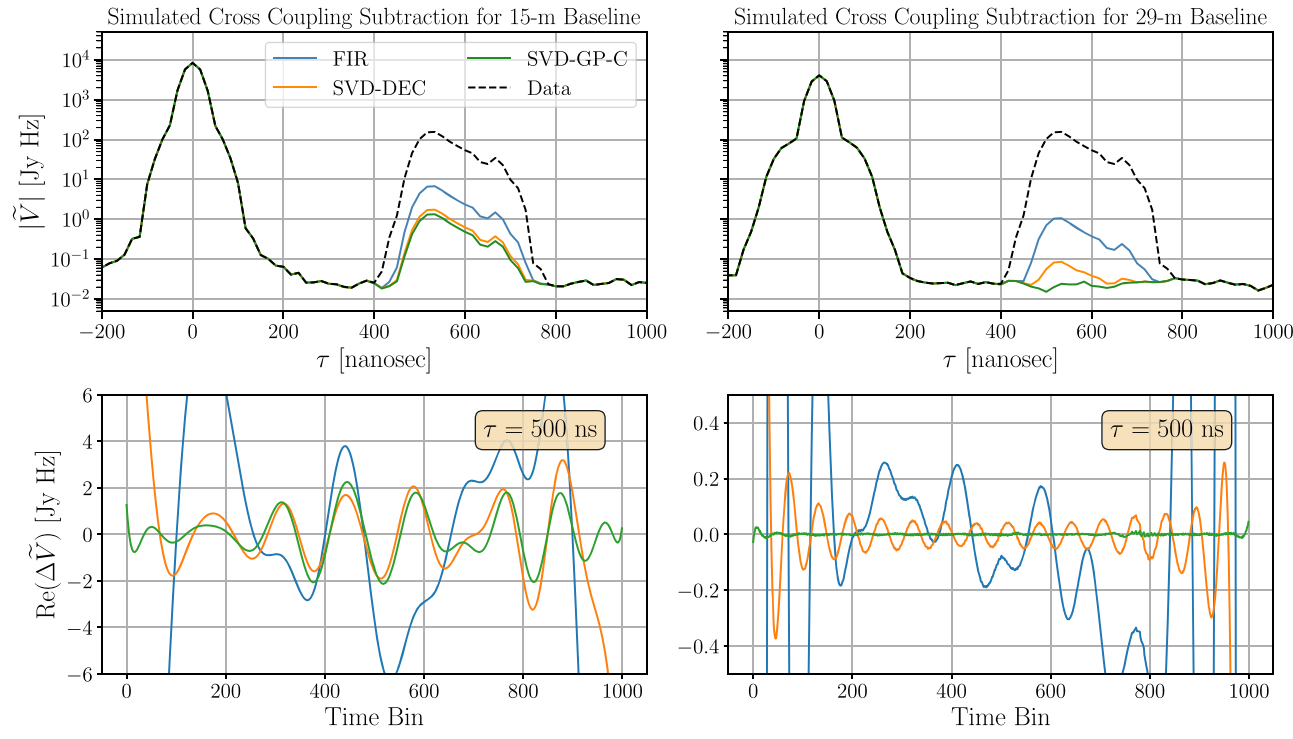


Figure 16. Cross-coupling removal comparison test for a FIR filter model, an SVD model with deconvolution low-pass filtering (SVD-DEC), and an SVD model with constrained-GP low-pass filtering (SVD-GP-C), applied to a 15 m baseline (left) and a 29 m baseline (right). The top panels show modeling and removal in delay space, and the bottom panels show the difference of each method's systematic model with the true systematic as a function of time, highlighting the severe boundary effects suffered by the FIR and SVD-DEC techniques.

generate 100 independent, uncorrelated complex Gaussian noise visibilities, compute our GP best-fit function given our fixed-length-scale hyper-parameter, and take its Fourier transform into fringe-rate space. We then take the absolute value of each Fourier transformed GP fit and average over the independent realizations. We do this for a GP with a $f_{\text{max}} = 1.0 \,\text{mHz}$ (GP) and for a GP with a more constrained cutoff of $f_{\text{max}} = 0.95 \,\text{mHz}$ (GP-C). The results are shown in Figure 15, showing that indeed the normal GP allows power slightly beyond its cutoff scale, whereas the constrained version with a 5% degraded cutoff diverges from the signal at the desired fringe rate. Therefore, when using a fixed-length-scale, squared-exponential GP as a low-pass filter, one should consider increasing the length-scale hyper-parameter by roughly 5% its nominal value in order to ensure that the filter is not allowing power beyond the desired fringe-rate scale.

Next we compare how the several techniques outlined here perform on simulated visibilities containing only foregrounds and a cross-coupling systematic. Our comparison will focus on three methods for building a cross-coupling visibility model: (1) a top-hat FIR filter that is 1 for all fringe-rate modes $|f| < f_{\rm max}$ and zero otherwise (labeled FIR), (2) the SVD-based method with a deconvolution low-pass filter applied to its T modes with a CLEAN boundary $|f| < f_{\rm max}$ (labeled SVD-DEC), and (3) the SVD-based method with a GP-C low-pass filter applied to its T modes (labeled SVD-GP-C). The top panels in Figure 16 plots the corrupted foreground + EoR + systematic visibility (black line), with the systematic-subtracted visibility for each technique, for a 15 m baseline (left) and a 29 m baseline (right). The bottom panels plot the difference of each systematic model with the true systematic at a single delay

as a function of time. We can clearly see the boundary effects that most severely plague the FIR method, but also the SVD-DEC method as well. When the GP-C method brings the systematic down to EoR levels, it too suffers slightly from boundary effects, but they are significantly less prevalent than the boundary effects seen in the other techniques, highlighting one benefit of using a GP-based low-pass filter.

Appendix C Software

The analysis presented in this work relies heavily on the Python programming language (https://python.org), and Python software developed by HERA collaboration members. Here we provide a list of these packages and their version or Git hash: aipy [v2.1.12] (https://github.com/HERA-Team/aipy), healvis [v1.0.0] (https://github.com/RadioAstronomy SoftwareGroup/healvis; Lanman & Pober 2019), hera_cal [v2.0] (https://github.com/HERA-Team/hera_cal), hera_ sim [v0.0.1] (https://github.com/HERA-Team/hera_sim), pyuvdata [v1.3.6] (https://github.com/RadioAstronomy SoftwareGroup/pyuvdata; Hazelton et al. 2017), and uvtools [v0.1.0] (https://github.com/HERA-Team/uvtools). These packages in turn rely heavily on other publicly available software packages, including: astropy [v2.0.14] (https:// astropy.org; The Astropy Collaboration et al. 2013), healpy [v1.12.9] (https://github.com/healpy/healpy), h5py [v2. 8.0] (https://www.h5py.org/), matplotlib [v2.2.4] (https://matplotlib.org), numpy [v1.16.2] (https://www. numpy.org), scipy [v1.2.1] (https://scipy.org), and scikit-learn [v0.19.2] (https://scikit-learn.org).

ORCID iDs

Nicholas S. Kern https://orcid.org/0000-0002-8211-1892 Joshua S. Dillon https://orcid.org/0000-0003-3336-9958

References

```
Ali, Z., Parsons, A., Zheng, H., et al. 2015, ApJ, 809, 61
Barry, N., Hazelton, B., Sullivan, I., Morales, M., & Pober, J. 2016, MNRAS,
Beardsley, A., Hazelton, B., Sullivan, I., et al. 2016, ApJ, 833, 102
Bowman, J. D., Rogers, A. E. E., Monsalve, R. A., Mozdzen, T. J., &
   Mahesh, N. 2018, Natur, 555, 67
Chaudhari, S. C., Gupta, Y., Kumar, A., et al. 2017, JAI, 6, 1641017
Cheng, C., Parsons, A. R., Kolopanis, M., et al. 2018, ApJ, 868, 26
de Oliveira-Costa, A., Tegmark, M., Gaensler, B. M., et al. 2008, MNRAS,
   388, 247
DeBoer, D., Parsons, A., Aguirre, J., et al. 2017, PASP, 129, 45001
Dillon, J., Liu, A., Williams, C., et al. 2014, PhRvD, 89, 23002
Efron, B., & Tibshirani, R. 1994, An Introduction to the Bootstrap (London:
   Taylor and Francis)
Ewall-Wice, A., Dillon, J., Hewitt, J., et al. 2016, MNRAS, 460, 4320
Ewall-Wice, A., Dillon, J. S., Liu, A., & Hewitt, J. 2017, MNRAS, 470, 1849
Fagnoni, N., de Lera Acedo, E., DeBoer, D. R., et al. 2019, arXiv:1908.02383
Furlanetto, S., Oh, S., & Briggs, F. 2006, PhR, 433, 181
Górski, K. M., Hivon, E., Banday, A. J., et al. 2005, ApJ, 622, 759
Greig, B., & Mesinger, A. 2015, MNRAS, 449, 4246
Greig, B., & Mesinger, A. 2018, IAUS, 333, 18
Greig, B., Mesinger, A., & Koopmans, L. 2015, arXiv:1509.03312
Hamaker, J. P., Bregman, J. D., & Sault, R. J. 1996, A&AS, 117, 137
Hazelton, B. J., Jacobs, D. C., Pober, J. C., & Beardsley, A. P. 2017, JOSS, 2, 140
Hogan, C., & Rees, M. 1979, MNRAS, 188, 791
Högbom, J. A. 1974, A&AS, 15, 417
Jacobs, D., Pober, J., Parsons, A., et al. 2015, ApJ, 801, 51
```

```
Kern, N., Parsons, A. R., Dillon, J. S., et al. 2019, arXiv:1909.11733
Kern, N. S., Liu, A., Parsons, A. R., Mesinger, A., & Greig, B. 2017, ApJ,
   848, 23
Koopmans, L., Pritchard, J., Mellema, G., et al. 2015, in Advancing
   Astrophysics with the Square Kilometre Array, ed. T. L. Bourke et al.
   (Trieste: PoS), 1
Lanman, A. E., & Pober, J. C. 2019, MNRAS, 487, 5840
Liu, A., & Parsons, A. 2016, MNRAS, 457, 1864
Madau, P., Meiksin, A., & Rees, M. 1997, ApJ, 475, 429
Mesinger, A (ed) (ed.) 2016, Understanding the Epoch of Cosmic Reionization:
   Challenges and Progress 4 (Cham: Springer), 23
Mesinger, A., Furlanetto, S., & Cen, R. 2011, MNRAS, 411, 955
Mouri Sardarabadi, A., & Koopmans, L. V. E. 2019, MNRAS, 483, 5480
Orosz, N., Dillon, J. S., Ewall-Wice, A., Parsons, A. R., & Thyagarajan, N.
   2019, MNRAS, 487, 537
Paciga, G., Albert, J., Bandura, K., et al. 2013, MNRAS, 433, 639
Parsons, A., Liu, A., Aguirre, J., et al. 2014, ApJ, 788, 106
Parsons, A., Pober, J., Aguirre, J., et al. 2012, ApJ, 756, 165
Parsons, A. R., & Backer, D. C. 2009, AJ, 138, 219
Parsons, A. R., Backer, D. C., Foster, G. S., et al. 2010, AJ, 139, 1468
Parsons, A. R., Liu, A., Ali, Z. S., & Cheng, C. 2016, ApJ, 820, 51
Patil, A., Yatawatta, S., Koopmans, L., et al. 2017, ApJ, 838, 65
Pober, J., Liu, A., Dillon, J., et al. 2014, ApJ, 782, 66
Pritchard, J., & Loeb, A. 2012, RPPh, 75, 86901
Rasmussen, C. E., & Williams, C. K. I. 2006, Gaussian Processes for Machine
   Learning (Cambridge, MA: MIT Press)
Sault, R. J., Hamaker, J. P., & Bregman, J. D. 1996, A&AS, 117, 149
Shaw, J. R., Sigurdson, K., Pen, U.-L., Stebbins, A., & Sitwell, M. 2014, ApJ,
Smirnov, O. M. 2011, A&A, 527, A106
Tauscher, K., Rapetti, D., Burns, J. O., & Switzer, E. 2018, ApJ, 853, 187
The Astropy Collaboration, A., Robitaille, T. P., Tollerud, E. J., et al. 2013,
   A&A, 558, A33
Tozzi, P., Madau, P., Meiksin, A., & Rees, M. 2000, ApJ, 528, 597
Zheng, H., Tegmark, M., Buza, V., et al. 2014, MNRAS, 445, 1084
```